Understanding influence of ocean waves on Arctic sea ice simulation: A modeling study with an atmosphere-ocean-wave-sea ice coupled model

Chao-Yuan Yang[1], Jiping Liu[2, 1], Dake Chen[1]

[1]Southern Marine Science and Engineering Guangdong Laboratory (Zhuhai), Zhuhai, Guangdong, China

[2]School of Atmospheric Sciences, Sun Yat-sen University, Zhuhai, Guangdong, China

Corresponding authors:
Chao-Yuan Yang (yangchaoyuan@sml-zhuhai.cn) and Jiping Liu (liujp63@mail.sysu.edu.cn)

Abstract

Rapid decline of Arctic sea ice has created more open water for ocean wave development and highlighted the importance of wave-ice interactions in the Arctic. Some studies have made contributions to our understanding of the potential role of the prognostic floe size distribution (FSD) on sea ice changes. However, these efforts do not represent the full interactions across atmosphere, ocean, wave, and sea ice. In this study, we implement a modified joint floe size and thickness distribution (FSTD) in a newly-developed regional atmosphere-ocean-wave-sea ice coupled model and conduct a series of pan-Arctic simulation with different physical configurations related to FSD changes, including FSD-fixed, FSD-varied, lateral melting rate, wave-fracturing formulation, and wave attenuation rate. Firstly, our atmosphere-ocean-wave-sea ice coupled simulations show that the prognostic FSD leads to reduced ice area due to enhanced ice-ocean heat fluxes, but the feedbacks from the atmosphere and the ocean partially offset the reduced ice area induced by the prognostic FSD. Secondly, lateral melting rate formulations do not change the simulated FSD significantly, but they influence the flux exchanges across atmosphere, ocean, and sea ice and thus sea ice responses. Thirdly, the changes of FSD are sensitive to the simulated wave height, wavelength, and wave period associated with different wave-fracturing formulations and wave attenuation rates, and the limited oceanic energy imposes a strong constraint on the response of sea ice to FSD changes. Finally, our results also demonstrate that wave-related physical processes can have impacts on sea ice changes with the constant FSD, suggesting the indirect influences of ocean waves on sea ice through the atmosphere and the ocean.

1. Introduction

Arctic sea ice, a major component in the climate system, has undergone dramatic changes over the past few decades associated with global climate change. September and March Arctic sea ice extent show decreasing trends of -13.1% and -2.6% per decade from 1979 to 2020, respectively (Perovich et al., 2020). The mean Arctic sea ice thickness has decreased by ~1.5-2 meters from the submarine period (1958-1976) to the satellite period (2011-2018), largely resulting from the loss of multiyear ice (Kwok, 2018; Tschudi et al., 2016). The drifting speed of Arctic sea ice exhibits an increasing trend based on satellite and buoy observations (e.g., Rampal et al., 2009; Spreen et al., 2011; Zhang et al., 2022). As the Arctic Ocean has been dominated by thinner and younger ice, Arctic sea ice is more likely to be influenced by forcings from the atmosphere and the ocean.

Associated with the above Arctic sea ice changes, the Arctic fetch (open water area for ocean wave development) is less limited by the ice cover. Previous studies suggested that the Arctic fetch and surface wind speed over the ice-free ocean correlate well with wave heights in the Arctic Ocean (Casas-Prat and Wang, 2020; Dobrynin et al., 2012; Liu et al., 2016; Stopa et al., 2016; Waseda et al., 2018). The higher ocean waves are more likely to propagate deeper into the ice pack and have sufficient energy to break sea ice into smaller floes (e.g., Kohout et al., 2014). The ice pack, with the same concentration, has larger surface area for the ice floes with smaller sizes, particularly lateral surfaces. The increased lateral surface accelerates ice melting through enhanced ice-ocean heat fluxes (e.g., Steele, 1992). Some studies also showed that the ice-floe melting rate is associated with the horizontal mixing of oceanic heat across ice floe edge between open water and under-floe ocean by oceanic eddies, in particular sub-mesoscale eddies, and the strength of this effect depends on floe size (Gupta and Thompson, 2022; Horvat et al., 2016). The enhanced ice melting creates more open water (i.e., fetch), which is a favorable condition for further wave development as well as the ice-albedo feedback (Curry et al., 1995). These processes create a potential feedback loop between ocean waves and sea ice (e.g., Asplin et al., 2014; Thomson and Rogers, 2014).

Arctic cyclones and their high surface wind are the important drivers for large wave events in the Arctic Ocean. Previous studies showed that intense storms like the "Great Arctic Cyclone" of 2012 (Simmonds and Rudeva, 2012) and a strong summer cyclone in 2016 could be one of the contributors to the anomalously low sea ice extent in 2012 and 2016 (e.g., Lukovich et al., 2021; Parkinson and Comiso, 2013; Peng et al., 2021; Stern et al., 2020; Zhang et al., 2013). Statistical analyses based on cyclone-tracking algorithm across multiple reanalyses suggested that the number of Arctic cyclones shows a significantly positive trend in the cold season (e.g., Sepp and Jaagus, 2011; Valkonen et al., 2021; Zahn et al., 2018). The increased cyclone activities and more open water areas cause more extreme wave events in the Arctic (e.g., Waseda et al., 2021). Blanchard-Wrigglesworth et al. (2021) found that extreme changes in Arctic sea ice extent are correlated with distinct wave conditions during the cold season based on the observations.

The potential feedback loop associated with ocean waves and sea ice and more extreme wave events indicates the importance of representing these processes in climate models for improving sea ice simulation and prediction (e.g., Collins et al., 2015; Kohout et al., 2014).

However, state-of-the-art climate models participating in the latest Coupled Model Intercomparison Project Phase 6 (CMIP6) have not incorporated the interactions between ocean waves and sea ice in their model physics (e.g., Horvat, 2021). The coupled effects of ocean waves and sea ice also include the decay of amplitude of ocean waves as they travel under the ice cover due to the combination of scattering and dissipation. (e.g., Squire, 2020). Crests and troughs of ocean waves exert strains on sea ice, and sea ice breaks if the maximum strain exceeds a certain threshold (e.g., Dumont et al., 2011). The wave-induced ice-breaking changes the size of floes, which in turn changes the floe size distribution (FSD; Rothrock and Thorndike, 1984). In addition to the interactions between ocean waves and sea ice, the floe size contributes to the changes in the atmospheric boundary layer (e.g., Schäfer et al., 2015; Wenta and Herman, 2019), mechanical responses of sea ice (e.g., Vella and Wettaufer, 2008; Weiss and Dansereau, 2017; Wilchinsky et al., 2010), the flux exchanges across air-sea ice-ocean interfaces (Cole et al., 2017; Loose et al., 2014; Lu et al., 2011; Martin et al., 2016; Steele et al., 1989; Tsamados et al., 2014), and the scattering of ocean wave propagation (e.g., Montiel et al., 2016; Squire and Montiel, 2016). Thus, it is essential to have a prognostic FSD to properly reflect wave-ice interactions as well as other processes related to the floe size in climate models.

Recently, several studies have made contributions on understating responses of sea ice to the prognostic FSD (e.g., Bateson et al., 2020; Bennetts et al., 2017; Boutin et al., 2020; Horvat and Tziperman, 2015; Roach et al., 2018a, 2019; Zhang et al., 2015, 2016). However, these studies used simplified model complexity (i.e., standalone sea ice model, ice-wave coupling, ice-ocean coupling) and were unable to give a full representation of sea ice responses to the evolving states of atmosphere, ocean, and wave based on explicit model physics as well as feedbacks from sea ice to them. Motivated by this, here we introduce a newly-developed atmosphere-ocean-wave-sea ice coupled model, in which we implement physical processes that simulate the evolution of floe size distribution. We use this new coupled model to investigate the responses of sea ice to ocean waves, as well as interactions in the Arctic climate system. This paper is structured as follows. Section 2 provides an overview of the new coupled model, focusing on the wave component and the implementation of the prognostic FSD. Section 3 describes the design of numerical experiments and the related model configurations. Section 4 examines the responses of sea ice to wave-ice interactions with the prognostic FSD, as well as other ocean wave-related processes. Discussions and concluding remarks are provided in section 5.

2. Model description

The newly-developed atmosphere-ocean-wave-sea ice coupled model is based on Coupled Arctic Prediction System (CAPS, Yang et al., 2022), which consists of the Weather Research and Forecasting Model (WRF), the Regional Ocean Modeling System (ROMS), and the Community Ice CodE (CICE). The detailed description of each model component in CAPS is referred to Yang et al. (2020; 2022). In this section, we focus on newly-added features in CAPS as described below.

2.1. Wave model component

To represent wave-ice interactions, an ocean wave model is coupled into CAPS, which is the Simulating Waves Nearshore (SWAN). SWAN is a third-generation wave model and includes processes of diffraction, refraction, wave-wave interactions, and wave dissipation due to wave breaking, whitecapping, and bottom friction (Booij et al., 1999). Recently, the SWAN model has implemented wave dissipation due to sea ice based on an empirical formula, which is called IC4M2 (Collins and Rogers, 2017; Rogers, 2019). Specifically, the temporal exponential decay rate of wave energy due to sea ice is defined as,

$$S_{ice}/E = -2c_g k_i \quad (1)$$

where S_{ice} is the sink term induced by sea ice, E is the wave energy spectrum, and c_g is the group velocity. k_i is the linear exponential rate that is a function of frequency as follow,

$$k_i(f) = c_0 + c_1 f + c_2 f^2 + c_3 f^3 + c_4 f^4 + c_5 f^5 + c_6 f^6 \quad (2)$$

where c_0 to c_6 are the user-defined coefficients and their values as described in Section 3. In the SWAN model, both the wind source term S_{in}, and the sea ice sink term are scaled by sea ice concentration a_{ice}, which is provided by the CICE model through the coupler in CAPS,

$$S_{ice} \rightarrow a_{ice} S_{ice} \quad (3)$$

$$S_{in} \rightarrow (1 - a_{ice}) S_{in} \quad (4)$$

2.2. Prognostic FSD

For the prognostic FSD implemented in the CICE model, we follow the joint floe size and thickness distribution (FSTD; Horvat and Tziperman, 2015). The FSTD is defined as a probability distribution $f(r,h)drdh$. $f(r,h)$ represents the fraction of cell covered by ice with floe size between r and $r + \Delta r$, thickness between h and $h + \Delta h$, and the FSTD satisfies,

$$\int_{\mathcal{R}} \int_{\mathcal{H}} f(r,h)drdh = 1 \ (5)$$

The ice thickness distribution $g(h)$ (ITD; Thorndike et al., 1975), which is simulated by the CICE model, and the FSD $F(r)$, can be obtained by integrating the FSTD over all floe sizes and all ice thicknesses,

$$\begin{aligned} \int_{\mathcal{R}} f(r,h)dr &= g(h) \\ \int_{\mathcal{H}} f(r,h)dh &= F(r) \end{aligned} \quad (6)$$

Roach et al. (2018a) suggested the modified FSTD, $L(r,h)$, to preserve the governing equations of ITD in the CICE model, which satisfies,

$$\int_{\mathcal{R}} L(r,h)dr = 1 \ (7)$$

and

$$f(r,h) = g(h)\, L(r,h) \ (8)$$

As described in Roach et al. (2018a), the implementation of the modified FSTD ignores the two-way relationship between floe size, that is, physical processes associated with FSD changes (i.e., $L(r,h)$ changes) are independent across each ice thickness category. The governing equation of FSTD is defined as,

$$\frac{\partial f(r,h)}{\partial t} = -\nabla \cdot (f(r,h)\vec{v}) + \mathcal{L}_T + \mathcal{L}_M + \mathcal{L}_W \ (9)$$

The terms on the right-hand side represent advection, thermodynamics, mechanical, and wave-induced floe-fracturing processes. For these terms, except the last term $\mathcal{L}_W$, we follow the approach described in Roach et al. (2018a) and related values for coefficients as described in

Section 3. The formulations of $\mathcal{L}_W$ proposed by Horvat and Tziperman (2015) involve a random function to generate sub-grid scale sea surface elevation to determine how floes are fractured by ocean waves. As a consequence, simulations are not bitwise reproducible with the formulation including a random function. To avoid this issue, we propose different approaches for our implementation of FSTD as described below.

2.3. Floe fracturing by ocean waves

For the floe-fracturing term $\mathcal{L}_W$, we follow the formulation suggested by Zhang et al. (2015), which has similar form as Horvat and Tziperman (2015) and can be described as,

$$\mathcal{L}_W = -Q(r)\,f(r,h) + \int_{\mathcal{R}} \beta(r',r)Q(r')f(r',h)dr' \quad (10)$$

The first term on the right-hand side represents the areal fraction reduction due to floe-fracturing and the second term is the areal fraction gain from other floe size categories that have floe-fracturing. In equation (10), $Q(r)$ is the probability that floe-fracturing occurs for floe size between r and $r + \Delta r$, and $\beta(r',r)$ is the redistributor that transfers fractured floe from floe size r' to r. $\mathcal{L}_W$ does not create or destroy ice so it must satisfy,

$$\int_{\mathcal{R}} \mathcal{L}_W dr = 0 \quad (11)$$

In this study, we propose two different formulations for $Q(r)$ and $\beta(r',r)$.

(a) Equally-redistribution

We follow the same assumption in Zhang et al. (2015). That is, ice-fracturing by ocean waves is likely to be a random process and the size of fractured floe does not have favored floe size based on aerial photographs and satellite images (e.g., Steer et al., 2008; Toyota et al., 2006, 2011). Thus, fractured floe is equally-redistributed into smaller floe sizes. The redistributor is defined as,

$$\beta(r_1, r_2) = \begin{cases} 1/(c_2 r_1 - c_1 r_1) & if\ c_1 r_1 \leq r_2 \leq c_2 r_1 \\ 0 & if\ \ r_2 < c_1 r_1\ or\ r_2 > c_2 r_1 \end{cases} \quad (12)$$

where c_1 and c_2 are constants that define upper- and lower-bound of floe size redistribution. Details of $\beta(r', r)$ in this formulation are referred to Zhang et al. (2015).

For the probability $Q(r)$, Zhang et al. (2015) used a user-defined coefficient to reflect wave conditions and determine $Q(r)$. Zhang et al. (2016) suggested that the coefficient is a function of wind speed, fetch, ITD, and FSD. Since CAPS has a wave component to simulate wave conditions, we reformulate $Q(r)$ to include simulated wave information from the coupler, and $Q(r)$ is defined as,

$$Q(r) = c_w H(\varepsilon) exp\left[-\propto \left(\frac{1-r}{r_{max}}\right)\right] \quad (13)$$

where $H(\varepsilon)$ is the Heaviside step function, the exponential function determines the fraction of each floe size participating in fracturing, and user-defined coefficients, c_w and $\propto$, control the upper-bound of $Q(r)$ and the shape of the exponential function. To include wave conditions from the SWAN model, we apply the floe-fracturing parameterization suggested by Dumont et al. (2011) to calculate the strain induced by ocean waves on ice floes, and use this parameterization to define $H(\varepsilon)$ as,

$$H(\varepsilon) = \begin{cases} 1, & if\ \varepsilon \geq \varepsilon_c \\ 0, & if \varepsilon < \varepsilon_c \end{cases} \quad (14)$$

$$\varepsilon = \frac{2\pi^2 h_{ice} A_{wave}}{{L_{wave}}^2} \quad (15)$$

where the strain ε is proportional to the ice thickness h_{ice} and the mean amplitude of wave A_{wave}, and inversely proportional to the square of the mean surface wavelength L_{wave}. If the strain exceeds the strain yield limit ε_c (see Section 3), floe-fracturing occurs (i.e., $H(\varepsilon) = 1$). The distribution of wave heights is, in general, a Rayleigh distribution, which allows us to use the simulated significant wave height from the SWAN model to determine the mean wave amplitude with the following relationship (e.g., Bai and Bai, 2014),

$$A_{wave} = \frac{H_{wave}}{2} \cong \frac{5}{16} H_s \quad (16)$$

where H_{wave} is the mean wave height, and H_s is the significant wave height.

The exponential function is built on that the wave strain on ice floes is separated by the wavelength (e.g., Dumont et al., 2011, their Fig. 4). Floe size smaller than the wavelength is more likely to move along with ocean waves with little bending (e.g., Meylan and Squire, 1994). That is, the exponential function preferentially has a higher fraction for larger floes.

(b) Redistribution based on a semi-empirical wave spectrum

As discussed in Dumont et al. (2011, their Fig. 4), fractured floes have a maximum size with half of the surface wavelength. Thus, the wave distribution of different wavelengths in each grid cell allows us to predict floe sizes after fracturing. The sea surface elevation is a result of the superimposition of waves with different periods, amplitudes, and directions in space and time. Empirical wave spectra have been proposed to describe wave conditions with a finite set of parameters. Based on wave observations from a wide variety of locations, Bretschneider (1959) suggested the formulation of wave spectrum, which is used to formulate the redistribution of fractured floe as described below.

The Bretschneider wave spectrum is defined as,

$$S_B(T) = \frac{1.25{H_s}^2 T^5}{8\pi {T_p}^4} exp\left[-1.25\left(\frac{T}{T_p}\right)^4\right] \quad (17)$$

where T_p is the peak wave period, and the spectral wave amplitude is defined as (Dumont et al., 2011),

$$A(T) = \sqrt{\frac{4\pi S_B(T)}{T}} \quad (18)$$

Similar to the distribution of wave height, Bretschneider (1959) found that the distribution of wave period is, in general, a Rayleigh distribution and defined as,

$$P(T) = 2.7\left(\frac{T}{T_{ave}}\right)^3 exp\left[-0.675\left(\frac{T}{T_{ave}}\right)^4\right] \quad (19)$$

where T_{ave} is the mean surface period. With the deep-water surface wave dispersion relation $L(T) = gT^2/2\pi$, the corresponding wave length for each wave period bin can be obtained, and the wave-strain distribution can be calculated with the modified equation (15),

$$\varepsilon(T) = \frac{2\pi^2 h_{ice} A(T)}{L(T)^2} \quad (20)$$

Combined with the Heaviside step function defined in the equation (14), the probability of floe-fracturing for each wave period is obtained,

$$P_f(T) = H\big(\varepsilon(T)\big)\overline{P}(T) \quad (21)$$

where $\overline{P}(T)$ is the normalized $P(T)$. Based on $P_f(T)$ and the assumption that fractured floes have a maximum size with half of the surface wavelength, the redistributor $\beta(r_1, r_2)$ can be obtained based on following criteria: 1) floe size between r and $r + \Delta r$ (in radius) must be greater than half of wavelength $L(T)$, 2) floes fractured by the wavelength $L(T)$ have the size of $L(T)/2$, and 3) $P_f(T)$ represents the fraction of floe with r and $r + \Delta r$ transferred to new size with r' and $r' + \Delta r$ determined by the criterion (2). The probability $Q(r)$ is the summation of $P_f(T)$ and represents the total fraction of floe participating in wave-fracturing.

3. Model configurations and experiment designs

The WRF, ROMS, SWAN, and CICE models use the same model grid with 320 (440) x- (y-) grid points and ~24km horizontal resolution (Fig. 1). Initial and boundary conditions for the WRF, ROMS, CICE models are generated from the Climate Forecast System version 2 (CFSv2, Saha et al., 2014) operational analysis, archived by National Centers for Environmental Information (NCEI), National Oceanic and Atmospheric Administration (NOAA). In our configurations, the SWAN model starts with the calm wave states (i.e., zero wave energy in all frequencies). The modified FSTD, $L(r, h)$, is initialized based on the power-law distribution of floe number, $N(r) \propto r^{-a}$ (e.g., Toyota et al., 2006), with the exponent a as 2.1 for all grid cells. Physical parameterizations of each model component are mostly identical to those used in Yang et al. (2022) and summarized in Table 1.

Cassano et al. (2011) suggested that the use of a higher model top (10 mb) or applying spectral nudging in the upper model levels leads to significantly reduced bases in pan-Arctic atmospheric circulation in the standalone WRF model. Thus, compared with Yang et al. (2022), we change the model top of the WRF model in CAPS from 50 mb to 10 mb. With coupling to the SWAN model in CAPS, the corresponding configurations are modified to reflect wave effects on the atmosphere and the ocean. In the Mellor-Yamada-Nakanishi-Niino planetary boundary layer scheme (MYNN; Nakanishi and Nino, 2009), the surface roughness, z_0, is modified to include the effect of waves based on the following formulation,

$$z_0 = 1200 H_s \left(\frac{H_s}{L_{wave}}\right)^{4.5} + \frac{0.11\upsilon}{u_*} \quad (22)$$

where υ is the viscosity, and u_* is the friction velocity (Taylor and Yelland, 2001; Warner et al., 2010). For the interaction of ocean waves and currents, the vortex-force (VF) formulation is applied that represents conservative (e.g., vortex and Stokes-Coriolis forces) and non-conservative wave effects. The non-conservative wave effects in the VF formulation include wave accelerations for currents and wave-enhanced vertical mixing (Kumar et al., 2012; Uchiyama et al., 2010). The dissipated wave energy due to surface wave breaking and whitecapping is transferred to the ocean surface layer as additional turbulent kinetic energy, which in turn enhances the vertical mixing. For the effect of currents on the dispersion relation in wave propagation, we employ a depth-weighted current to account for the vertically-sheared flow following Kirby and Chen (1989). As discussed in previous studies (e.g., Naughten et al., 2017; Yang et al., 2022), the upwind third-order advection (U3H, Table 1) scheme, which is an oscillatory scheme, can lead to increased non-physical frazil ice formation. To address this issue, we implement the upwind flux limiter suggested by Leonard and Mokhtari (1990) to reduce false extrema caused by the oscillatory behavior of the U3H scheme. The value of yielding strain ε_c, described in Section 2.3 is chosen as $\cong 3 \times 10^{-5}$ (Dumont et al., 2011; Horvat and Tzipermann, 2015; Langhorne et al., 1998). The floe welding parameter in the thermodynamic term $\mathcal{L}_T$, is chosen as $1 \times 10^{-7}\ km^{-2}s^{-1}$. Roach et al. (2018b) found a lower bound of floe welding parameter as $1 \times 10^{-9}\ km^{-2}s^{-1}$ in the autumn Arctic based on the observations. Also, the floe welding process only occurs in the freezing condition (Roach et al., 2018a), and the freezing condition is determined by net ice mass increase by thermal mass change (see Figure 3). The floe welding parameter will behave like a step function during the freeze-thaw transition. For the user-defined coefficients in equation (4), all experiments use the equally-redistributed formulation described in Section 2.3 with c_w as 0.8 and $\propto$ as 1.0. Based on the formation of $\mathcal{L}_T$ in the equation (9) (see Roach et al., 2018a), the floe size change through the lateral surface is determined by both the floe size and the lateral melting rate. In the existing sea ice models, the lateral melting rate w_{lat} is all based on the empirical formulation suggested by Perovich (1983, hereafter P83),

$$w_{lat} = m_1 \Delta T^{m_2} \ (23)$$

where ΔT is the temperature difference between sea surface temperature (SST) and the freezing point, and m_1, m_2 are empirical coefficients based on the observations from a single sea ice lead in the Canadian Arctic. This empirical formulation is also the default lateral melting rate in the CICE model. Maykut and Perovich (1987, hereafter MP87) showed a different approach to parameterize the lateral melting rate that includes the friction velocity u_* based on the observations from the Marginal Ice Zone Experiment, which is defined as,

$$w_{lat} = u_* m_3 \Delta T^{m_4} \ (24)$$

Both formulations (Equ. 23, 24) are examined in this study (see Table 2). In the equation (2), the user-defined coefficients for the wave attenuation are set as $c_2 = 1.06 \times 10^{-3}$ and $c_4 = 2.3 \times 10^{-2}$ (case 1), which follow the polynomial of Meylan et al. (2014, hereafter M14) from the observations with 10-25m floe in diameter in the Antarctic, and $c_2 = 2.84 \times 10^{-4}$ and $c_4 = 1.53 \times 10^{-2}$ (case 2), which follow the polynomial of Rogers et al. (2018, hereafter R18) based on the observations for pancake and frazil ice in the Arctic.

In this study, a series of numerical experiments for the pan-Arctic sea ice simulation have been conducted, starting from January 1st, 2016 to December 31st, 2020. Table 2 provides the details of the configurations for these experiments, which allow us to examine the influence of ocean waves and related physical processes on Arctic sea ice simulation in the atmosphere-ocean-wave-sea ice coupled framework. Specifically, these experiments focus on 1) the comparison between constant FSD and prognostic FSD (Exp-CFSD and Exp-PFSD), 2) sea ice responses to different lateral melting rate parameterizations (Exp-CFSD, Exp-PFSD, Exp-LatMelt-C and Exp-LatMelt-P), 3) the difference between the equally-redistributed formulation and the Bretschneider formulation for floe fracturing (Exp-PFSD and Exp-WaveFrac-P), and 4) the contribution of different wave attenuation rates to sea ice changes (Exp-CFSD, Exp-PFSD, Exp-WaveAtt-C and Exp-WaveAtt-P).

4. Results

4.1 Constant vs. Prognostic floe size

Figure 2 shows the evolution of sea ice area (SIA) for all experiments conducted in this study (as well as the values of seasonal maximum and minimum SIA for all experiments are summarized in Table S1). SIA is calculated as the sum of the ice-covered area of all grid cells (cell-area times sea ice concentration). In addition to the evolution of SIA, the 2016-2020 averaged March and September sea ice concentration (SIC) for all experiments are shown in Figure S1. Compared with Exp-CFSD, which uses a constant floe diameter (300m) in the lateral melting scheme (Steele, 1992), Exp-PFSD uses the equations described in Section 2.2 to determine the prognostic FSD and related physical processes (see Table 2). With the prognostic FSD, the evolution of SIA in Exp-PFSD (Fig. 2a, red line) shows smaller SIA in the melting months (June to September) and similar magnitude of SIA in other months compared to that of Exp-CFSD (Fig. 2a, blue line) during 2016-2018. After that, Exp-PFSD simulates smaller SIA than that of Exp-CFSD for most months during 2019-2020, especially for the seasonal maximum of 2019 and SIA after May 2020.

Figure 3 shows the evolution of sea ice mass budget terms with cell-area weighted averaging over the entire model domain with a 15-day running-average for smoothing out high-frequency fluctuations for all experiments. The most notable difference between Exp-CFSD and Exp-PFSD is the magnitude of basal melt (red lines) and lateral melt (grey lines). In Exp-CFSD, basal melt plays the dominant role in reducing sea ice mass compared to lateral melt which has negligible contribution to the total mass change. As discussed in Maykut and Perovich (1987), the inclusion of friction velocity in calculating the lateral melting rate results in $w_{lat} \rightarrow 0$ as $u_* \rightarrow 0$, which contributes to negligible lateral melt in Exp-CFSD. By contrast, Exp-PFSD with prognostic floe size shows that lateral melt has the major contribution in reducing ice mass (Fig. 3b), a result of smaller floe size near the ice edge simulated by Exp-PFSD (Fig. 10a). It is also notable that the increased lateral melt in Exp-PFSD tends to be compensated by the decreased basal melt (Fig. 3b). The overall ice melt due to oceanic processes in Exp-PFSD (i.e., the sum of lateral melt and basal melt) does not change significantly compared to that of Exp-CFSD (Fig. S2e). The melting potential in the CICE model of CAPS, the available energy from the ocean to melt sea ice, is defined as the vertical integral of the difference between ocean temperature and freezing point within the surface layer (to 5-meter depth in CAPS) from the ROMS model. When the available oceanic energy is less than the sum of heat fluxes used for lateral and basal melt, the CICE model performs a linear scaling to maintain the relative magnitude of heat fluxes for lateral and basal melt. Thus, the increased energy consumption by lateral melt due to smaller floe size reduces the available energy for basal melt. Such change between lateral and basal melt has been shown in some studies (e.g., Bateson et al., 2020, 2022; Roach et al., 2018a, 2019; Smith et al., 2022; Tsamados et al., 2015). Although the rough compensation, Exp-PFSD simulates more ice melted by the oceanic energy compared to Exp-CFSD from January to July (Fig. S2e).

Figure 4 shows the evolution of ice-ocean heat flux, the friction velocity at the ice-ocean interface, and the temperature difference between SST and freezing point for Exp-CFSD and Exp-PFSD. These variables are the average of ice-covered cells with at least 1% ice concentration, and the ice-ocean heat flux is weighted by the ice concentration so that the weighted heat flux represents the mean value of the cell, rather than the mean value of the ice-ocean interface. It should be noted that cells with negative values of the temperature difference (i.e., supercooled water) are forced to be zero. This is consistent with the treatment in the CICE model for the calculation of ice-ocean heat flux. As shown in Fig. 4a and Fig. S2e, the evolution of ocean-induced ice melt is consistent with that of the ice-ocean heat flux for both Exp-CFSD and Exp-PFSD. Both Exp-CFSD and Exp-PFSD show relatively similar evolution of the friction velocity (Fig. 4b). The temperature difference of Exp-PFSD is much smaller than that of Exp-CFSD (Fig. 4c). The ice-ocean heat flux is the total heat flux from ocean to ice through ice bottom surface and lateral surface. Although Exp-PFSD has smaller temperature difference as well as the melting potential under ice-covered cells, the larger total ice surface area due to smaller floe size increases the efficiency of Exp-PFSD extracting energy from the ocean. The smaller temperature difference of Exp-PFSD and the compensation between lateral and basal melt suggest that the ocean surface layer of Exp-PFSD is closer to the freezing point compared to that of Exp-CFSD. Energy loss from the ocean through air-sea heat flux in winters that further cools the upper ocean, freshwater input (e.g., ice melting, precipitation) that raises the freezing point, as well as non-physical numerical oscillations (Naughten et al., 2017; Yang et al., 2022), are potential contributors that lead to increased frazil ice formation of Exp-PFSD as shown in Fig. 3a-b and Fig. S2g.

Figure 5 shows the heat flux budget at the ice surface averaged for all ice-covered cells. The positive ice-atmosphere heat fluxes of Exp-CFSD and Exp-PFSD in July (Fig. S3a) correspond to top melt in Fig. 3a-b and Fig. S2b (as well as Table S2). The ice-atmosphere heat flux not only determines the magnitude of ice surface melt in summer but also the energy loss from the ice interior in winter, which is crucial for ice growth. As shown in Fig. S3a, Exp-PFSD loses more energy to the atmosphere than that of Exp-CFSD in most winters. The conductive heat flux also shows similar evolution, suggesting that more energy is conducted to the ice top from ice layers below in Exp-PFSD (Fig. S3b). The loss of ice energy then contributes to increased ice growth at the ice bottom as shown in Fig. 3a-b and Fig. S2f (as well as Table S2). Generally, the net shortwave flux of Exp-PFSD is larger (ice gains more energy) than that of Exp-CFSD, especially during the melting season (Fig. S3c). In contrast to the net shortwave flux, for most of the time, the net longwave flux of Exp-PFSD is smaller (i.e., ice loses more energy) than that of Exp-CFSD (Fig. S3d). Exp-PFSD loses more energy through sensible heat flux compared to Exp-CFSD (Fig. S3e). For latent heat flux, there are no common features between Exp-PFSD and Exp-CFSD, suggesting the difference in the simulation of atmospheric transient systems (Fig. S3f).

The ice mass budget in Fig. 3 is not directly related to the evolution of SIA in Fig. 2 since each process acts differently in changing SIA. For vertical processes (i.e., top melt, basal melt), ice must be vertically-melted completely to reduce SIA. Lateral melt, on the contrary, can directly reduce SIA (Smith et al., 2022). Figure 6 shows the evolution of SIA changes due to thermal processes (top melt, basal melt, lateral melt, frazil ice formation) and dynamical processes (transport, ridging). For thermal area changes, Exp-PFSD (red line), in general, shows comparable ice area changes compared to Exp-CFSD (blue line) for most of the period (Fig. 6a). Compared with Fig. S2g, the timings that Exp-PFSD shows more thermally-increased ice area correspond to increased frazil ice formation, which primarily occurs in open water. In contrast to thermal area changes, dynamical area changes of Exp-PFSD tend to reduce ice area relative to that of Exp-CFSD (Fig. 6e). Dynamically-induced area changes are partly due to the ridging scheme (Lipscomb et al., 2007) that favors the conversion of thin ice to thicker ice and reduces total ice area but preserves the total volume. In general, Exp-PFSD has a higher fraction of ice in the thinner ITD range than Exp-CFSD.

Based on geographic features, we define the following subregions for further analysis: 1) Barents and Greenland Seas (ATL, 45W-60E, 65N-85N), 2) Laptev and Kara Seas (LK, 60E-150E, 65N-85N), and 3) Beaufort, Chukchi, and East Siberian Seas (BCE, 150E-120W, 65N-

85N, see black boxes in Fig. 1 for the geographic coverage of subregions). The fetches of ATL, LK, and BCE regions are limited by the surrounding continents and the seasonal evolution of ice-covered areas. The ATL region is only partially-limited by ice-covered areas while the LK and BCE regions can be fully-covered by sea ice in winter. Though these subregions also include part of the central Arctic Ocean, they will still be addressed by the main peripheral seas in the subregions in the following discussion for simplicity. Figure 7 shows the evolution of sea ice extent, sea ice area, domain-averaged significant wave height, melting potential, and heat flux at the ocean surface ($FLUX_{OCN}$, including ice-ocean and atmosphere-ocean interfaces) of Exp-CFSD and Exp-PFSD. As shown in Fig. 7a-i, it is clear that the higher (lower) significant wave height corresponds to less (more) regional ice coverage for all subregions. For the melting potential (Fig. 7j-l), the difference between Exp-CFSD (blue line) and Exp-PFSD (red line) in August, in general, is correlated with $FLUX_{OCN}$ in July (Fig. 7m-o). The more (less) incoming heat flux to the ocean due to less (more) ice-covered area increases (decreases) energy stored in the ocean surface layer. However, $FLUX_{OCN}$ alone cannot explain the difference in the melting potential for the entire period. For example, Exp-PFSD shows more melting potential after December 2019 in the ATL region (Fig. 7j), and more melting potential in December 2017 in the LK region (Fig. 7k) compared to Exp-CFSD. These timings do not show corresponding $FLUX_{OCN}$ in the preceding month, suggesting the contribution of different processes. Figure 8 shows the evolution of wave energy dissipation due to whitecapping and the difference of temperature profile in the upper 150m for Exp-CFSD and Exp-PFSD. As described in section 3, wave energy dissipation increases the turbulent kinetic energy in the surface layer and thus vertical mixing. Dissipation due to surface wave breaking is zero for most of the period. Occasionally, there are non-zero dissipations due to surface wave breaking for Exp-CFSD and Exp-PFSD. The evolution of wave dissipation due to whitecapping (Fig. 8a-c) is in good agreement with that of significant wave height in Fig. 7g-i. This suggests that stronger wave conditions associated with less ice-covered areas increase the effect of vertical mixing. Combined with the warmer upper ocean in Exp-PFSD after January 2020 in the ATL region and in December 2017 in the LK region in Fig. 8d-e, the strengthened vertical mixing brings warmer water of the subsurface upward and maintains/increases the melting potential in the subregions. Figure 8d-f also shows that the warmer signal in the upper ocean (at least to 60m depth) of Exp-PFSD persists after July 2018 in the ATL region while the LK and BCE regions show seasonal oscillation of ocean temperature in the upper ocean for the entire simulation. Combined with the regional SIA shown in Figure 7d-f, seasonal fully ice-covered states in the LK and BCE regions force the upper ocean to restore to certain states (i.e., near freezing point under sea ice, near zero melting potential shown in Fig. 7k-l) for both Exp-CFSD and Exp-PFSD, which might mitigate the effects of ocean wave activities and other processes on the upper ocean. With less restoring effect by sea ice on the upper ocean in the ATL region, the difference of thermally-induced mass change between Exp-PFSD and Exp-CFSD shows a larger variation once the upper ocean difference starts to persist after July 2018 (Fig. 8d, S4d) while the variations in the LK and BCE regions remain relatively unchanged for the entire simulation (Fig. S4e-f).

Additionally, atmospheric circulation responds to the changes in the spatial distribution of sea ice (Fig. S1). As shown in Figure S5, Exp-PFSD tends to have anomalous anti-cyclonic circulations in September compared to Exp-CFSD, but there is no consistent center of action during the entire period. In March, Exp-PFSD tends to simulate anomalous cyclonic circulations in the Barents-Kara Sea for most of the years compared to Exp-CFSD, except in 2019. The responses in the atmospheric state in both experiments also influence sea ice movement, which further contributes to the regional ice differences in Fig. 7a-f, as well as the heat flux budgets in Fig. S3.

4.2 Sensitivity to lateral melting rate parameterization

In addition to the floe size as discussed in the above section, the lateral melting rate (w_{lat}) is an important factor contributing to the relative strength of lateral and basal melt. As described in section 3, we conduct the experiments with the lateral melting rate suggested by Perovich (1983, P83), and Maykut and Perovich (1987, MP87) (see Table 2), to examine the sensitivity of Arctic sea ice simulation to different lateral melting rate parameterizations. As shown in Fig. 2b, the simulated summer sea ice area of Exp-LatMelt-C (green line) and Exp-LatMelt-P (grey line), in general, is larger than those of Exp-CFSD (blue line) and Exp-PFSD (red line).

As shown in the sea ice mass budget (Fig. 3a, 3c), Exp-LatMelt-C, which does not include the friction velocity in the formulation (Equ. 23), but keeps other model configurations same as Exp-CFSD only shows a slightly larger contribution to lateral melt during summer months (Fig. S6d). Also, the contribution to basal melt by Exp-LatMelt-C is generally smaller than that in Exp-CFSD (Fig. S6c). Similar to the experiments with the MP87 scheme, Exp-LatMelt-P with the prognostic FSD also shows the compensation between lateral melt and basal melt compared to Exp-LatMelt-C (Fig. 3c, 3d). Exp-LatMelt-P shows stronger lateral melt compared to Exp-PFSD, which is contributed by the P83 formulation (Fig. S6d). Despite the stronger lateral melt in Exp-LatMelt-P, its basal melt is smaller compared to Exp-PFSD (Fig. S6c). Thus, the ocean-induced melt of Exp-LatMelt-P is broadly similar to that of Exp-PFSD. The result of Exp-LatMelt-P and Exp-PFSD suggests that the changes in lateral and basal melt due to different lateral melting rate parameterizations are mostly controlled by the available energy from the ocean (i.e., melting potential).

Exp-LatMelt-P simulates more basal growth in winter (Fig. S6f), which is contributed by more energy loss to the atmosphere (Fig. 5a), in comparison to Exp-PFSD. Also, more frazil ice formation is simulated in Exp-LatMelt-P than Exp-PFSD during most of the simulation period (Fig. S6g). The combined effects of the above processes lead to Exp-LatMelt-P showing less total ice melt in summer and similar ice growth in winter compared to Exp-PFSD (Fig. S6a). Due to more frazil ice formation, Exp-LatMelt-P shows more thermally-increased ice area compared to Exp-PFSD (Fig. 6, Fig. S6g). Frazil ice formation reduces open-water areas and blocks the energy exchange between the atmosphere and the ocean. That is, the upper ocean under sea ice in Exp-LatMelt-P receives less incoming flux from the atmosphere (i.e., solar radiation) during April to September (not shown) to balance the energy consumption by ice melt, which leads to smaller ocean temperature difference compared to Exp-PFSD (Fig. 4c, green and red lines).

Figure 9 shows the spatial distribution of sea ice concentration, sea surface temperature, and friction velocity in September 2020 for the experiments using MP87 and P83 schemes.

Exp-CFSD, Exp-PFSD, and Exp-LatMelt-C simulate large areas with ice concentration less than 5% (they are mostly much less than 1%, Fig. 9a-c). In opposite to these three experiments, Exp-LatMelt-P does not show wide areas with non-zero and infinitesimal ice concentration (Fig. 9d). Although these areas only account for a tiny fraction of total sea ice, they may still be a source of uncertainty for sea ice simulations. Ice-existed cells can be influenced by all processes involved in sea ice mass budget (Fig. 3) while ice-free cells can only be affected by frazil ice formation and dynamical advection. Under these small-ice areas, SST is well above the freezing point (Fig. 9e-h) and the friction velocity is mostly less than $5 \times 10^{-4}\ m/s$ (Fig. 9i-l). In our configuration of the CICE model, the minimum value of friction velocity is set to $5 \times 10^{-4}\ m/s$. This suggests that the friction velocity is the limit factor for heat flux transferred into sea ice in the small-ice areas. For basal heat flux, the formulation in the CICE model is based on Maykut and McPhee (1995), which is controlled by the friction velocity and the temperature difference. Thus, basal heat fluxes with small friction velocities may not be large enough to satisfy the energy convergence (in conjunction with conductive heat flux at the ice bottom) at the ice-ocean interface to melt ice if the temperature difference does not show a larger magnitude. Since the MP87 scheme includes the friction velocity, lateral heat flux is also limited in small-ice areas. Exp-PFSD has a much smaller floe size (compared to 300m) in these small-ice areas, but the increased strength of lateral melt does not overcome the limitation of friction velocity to melt ice completely (Fig. 9b). The P83 scheme, which does not include the friction velocity, is controlled by the temperature difference, but the effect of lateral melting in Exp-LatMelt-C is largely constrained by constant 300m floe diameter. Liang et al. (2019)

suggested these small-ice areas can be eliminated by assimilating SST observations. The results of Exp-LatMelt-P suggest a model physic approach that considers the prognostic FSD and the lateral melting rate to reduce the coverage of small-ice near the ice-edge.

4.3 Sensitivity to floe-fracturing parameterization

The equally-redistributed formulation (hereafter PF1) for floe-fracturing described in section 2.3.a does not have preferential floe size after fracturing (i.e., a stochastic process). However, the size of fractured floes can be predicted based on the properties of surface ocean waves, particularly wavelength (Dumont et al. 2011; Horvat and Tziperman, 2015). In this section, we conduct an experiment (Exp-WaveFrac-P, see Table 2), which utilizes a semi-empirical wave spectrum to redistribute fractured floes (see section 2.3.b for details and hereafter PF2) to explore the effects of different wave-fracturing formulations on Arctic sea ice simulation. As shown in Fig. 2c, Exp-WaveFrac-P (orange line) simulates larger SIA in summer and comparable SIA in winter compared to that of Exp-PFSD (red line).

By applying different formulations for floe-fracturing (as well as different lateral melting rate formulations), the FSD responds accordingly. To quantify the responses of FSD associated with different physical configurations (Table 2), the representative floe radius r_a, as well as its tendency due to different processes in the equation (9) are utilized and calculated as (Roach et al., 2018a),

$$r_a = \frac{\int_{\mathcal{R}} \int_{\mathcal{H}} r f(r,h) dr dh}{\int_{\mathcal{R}} \int_{\mathcal{H}} f(r,h) dr dh} \quad (25)$$

$$\frac{dr_a}{dt} = \frac{\int_{\mathcal{R}} \int_{\mathcal{H}} r \frac{df(r,h)}{dt} drdh}{\int_{\mathcal{R}} \int_{\mathcal{H}} f(r,h) drdh} \quad (26)$$

Figure 10 shows the spatial distribution of the representative floe radius in winter and summer for all experiments with the prognostic FSD. As described in section 3, $L(r,h)$ is initialized by the power law distribution with the exponent as 2.1 for all experiments. Exp-WaveFrac-P shows a smaller floe radius in the Chukchi and East Siberian Seas and north of Greenland at the early stage of simulation compared to experiments using PF1 formulation (Fig. 10a-o, upper panel). Small-floe areas in Exp-WaveFrac-P are mostly contributed by the effect of wave-fracturing where decreasing tendency of floe radius can extend further into the central Arctic from the Atlantic and the Bering Strait compared to PF1 experiments (Fig. S7). After September 2016, the representative floe radii of PF experiments emerge, that is, Exp-WaveFrac-P has a smaller floe size compared to PF1 experiments for both winter and summer (Fig. 10a-o). In summer, Exp-WaveFrac-P shows mostly fully-fractured floe (<10m, Fig. 10k-o, bottom panel). The stronger wave-fracturing shown in Exp-WaveFrac-P is partly contributed by the semi-empirical wave spectrum used in PF2. The simulated wave parameters under ice-covered area are mostly with $H_s < 0.01\ m/s$ and $T_p > 15\ s$. The constructed wave spectrum and amplitude based on simulated wave parameters under sea ice and equations (17) and (18) still include the contribution from high-frequency waves ($T = 2s\ bin$), especially in the ice pack far from the ice edge. The high-frequency waves only account for a small fraction in the wave period distribution $\overline{P}(T)$, and have small wave amplitude $A(T)$ ($\sim 7 \times 10^{-4} m$). The strain of the high-frequency bin based on equation (20) still exceeds the yielding strain and then fractures ice floe into the smallest floe size category. Observational and numerical studies showed that high-frequency waves rapidly decay and reach the “zero” transmission state for high-frequency waves when traveling under sea ice (e.g., Collins et al., 2015; Liu et al., 2020). Despite the over-fracturing behavior shown in Exp-WaveFrac-P, the prevalence of small-floe does not translate into the stronger ocean-induced ice melt but weaker melt in summer compared to Exp-PFSD (Fig. 3d-e, Fig. S8e), indicating the limiting role of melting potential. The weaker ocean-induced ice melt in the summer of Exp-WaveFrac-P corresponds to smaller ice-ocean heat fluxes (Fig. S9a), which is contributed by both smaller friction velocity and temperature difference (Fig. S9b-c).

4.4 Sensitivity to wave-attenuation parameterization

We have shown that ocean waves can alter the upper ocean through wave-enhanced mixing, which may affect sea ice locally (Fig. 8, see section 4.1). The results from PF1 and PF2 experiments imply that the simulated wave parameters can determine how ice floes are fractured. As described in section 2.1, we can choose different coefficients in equation (2) to control the wave attenuation rate of each frequency. In this section, we conduct experiments using R18 coefficients (see section 3 and Table 2) to study the impacts of wave-attenuation rate on Arctic sea ice simulation. The simulated sea ice area in Exp-WaveAtt-C (Fig. 2d, light-blue line) resembles that in Exp-CFSD (Fig. 2d, blue line) before 2019. After 2019, Exp-WaveAtt-C simulates smaller SIA compared to Exp-CFSD. Since both Exp-CFSD and Exp-WaveAtt-C use constant floe size, which allows us to neglect the effect of the spatial distribution of floe size and the MP87 scheme, which makes lateral melt have a negligible contribution (Fig. S10d), basal melt is the primary factor for the ocean-induced ice melt during the entire period (Fig. 3a, 3f, and Fig. S10e). The strength of basal melt in Exp-WaveAtt-C is weaker than that in Exp-CFSD from April 2018 to January 2020 (Fig. S10c). Basal growth of Exp-WaveAtt-C is also smaller than that of Exp-CFSD in the winter of 2018 and 2019 (Fig. S10f). Compared to Exp-CFSD, Exp-WaveAtt-C shows stronger top melt in the summer of 2018 (Fig. S10b). The combined effects of the above processes lead to a thinner ice state in Exp-WaveAtt-C before 2019 (Fig. S10a). The thinner state of Exp-WaveAtt-C in the winter of 2019 causes more open water be created by basal melt (regardless of its smaller magnitude) and thus smaller SIA (Fig. 2d), which is also shown in the thermally-induced ice area changes that Exp-WaveAtt-C has smaller magnitude in the corresponded period (Fig. 6d). As discussed in section 4.1, top melt and basal growth is in good agreement with the ice-atmosphere heat flux (Fig. S10, S11a). That is, ice mass and area changes described above are mainly driven by the ice-atmosphere heat flux associated with the atmospheric responses to the changes in ocean wave conditions.

Different from the M14 experiments, the simulated SIA of Exp-WaveAtt-C (light-blue line) and Exp-WaveAtt-P (yellow line) show relatively similar evolution during 2016-2020 (Fig. 2d). The R18 coefficients represent weaker wave attenuation relative to the M14 coefficients. Thus, ocean waves in the R18 experiments are expected to transmit further into the ice pack while maintaining relatively higher wave energy. To quantify to what extent the ice can be affected by ocean waves, we calculate the wave-affected extent (WAE), which is defined as the sum of the area of cells with ice concentration greater than 15% and significant wave height greater than 30cm (Cooper et al., 2022). Figure 11 shows the evolution of WAE for the M14 and R18 experiments with a 15-day running average to smooth the high-frequency changes of wave conditions. The weaker attenuation in Exp-WaveAtt-C and Exp-WaveAtt-P results in generally larger WAE compared to Exp-CFSD and Exp-PFSD (as well as all previous experiments with M14 coefficients, not shown). The direct impact of larger WAE in Exp-WaveAtt-P is that the representative floe radius is mostly smaller than 10m (fully-fractured by ocean waves) (Fig. 10p-t). The decreasing tendency of floe radius due to wave-fracturing is the dominant factor contributing to the fully-fractured condition (Fig. S7). Similar to Exp-WaveFrac-P, the fully-fractured condition does not lead to stronger ocean-induced melt due to limited oceanic energy (Fig. 3b, 3e, 3g, S10e).

5. Conclusions and Discussions

This study investigates the impacts of ocean waves on Arctic sea ice simulation based on a newly-developed atmosphere-ocean-wave-sea ice coupled model, which is built on the Coupled Arctic Prediction System (CAPS) by coupling the Simulating Waves Nearshore (SWAN) and the implementation of the modified joint floe size and thickness distribution (FSTD). A set of pan-Arctic experiments with different configurations of FSD-related processes are performed for the period 2016-2020. Specifically, we examine the contrasting behaviors of sea ice between constant and prognostic floe size, the responses of sea ice to different lateral melting rate formulations, and the sensitivity of sea ice to the simulated wave parameters under the atmosphere-ocean-wave-sea ice coupled framework.

The results of FSD-fixed and FSD-varied experiments show that the simulated sea ice area is generally lower with smaller floe size associated with physical processes that change

FSD. According to sea ice mass budget analysis, smaller floe size contributes to increased lateral melt, but its effect is reduced by decreased basal melt. The combined effects of lateral and basal melt associated with smaller floe size result in relatively more ice melt by the ocean energy, which is similar to previous studies (e.g., Bateson et al., 2022; Roach et al., 2019; Smith et al., 2022). The simulations in Smith et al. (2022) with varying lateral melting strength based on the Community Earth System Model version 2 (CESM2) with a slab-ocean model showed minimal change in frazil ice formation. In our simulation with a full ocean model, the enhanced ice melt by the ocean, though it is partially balanced by increased frazil ice formation due to the depletion of melting potential in the surface layer. This suggests negative feedback from the full ocean physics. Our simulations also show that the prevalence of small floes does not necessarily lead to stronger ice melting due to limited oceanic energy. To further illustrate the constraint role of limited oceanic energy, the mixed layer depths (MLDs) based on 0.1 degree Celsius difference relative to the surface temperature (e.g., Courtois et al., 2017, their Table 2) for Exp-CFSD and Exp-PFSD are shown in Figure 12. In general, Exp-CFSD and Exp-PFSD (as well as other experiments, not shown) exhibit similar evolution of MLD, that is MLD is deeper (up to 150m) in March and shallower (up to 80m) in September. MLD in the open waters is broadly similar across all experiments and MLD near the ice edge (15% ice concentration, black contour in Fig. 12) is shallower (10-30m) relative to other areas. In March, MLDs under ice-covered areas become deeper as lead time increases. To calculate the heat content within MLD, the same approach for calculating melting potential in the ROMS model is used, which is defined as the vertical integral from the surface to MLD of the difference between ocean temperature and freezing point. The calculated values of heat content and melting potential have the same unit (W/m^2) and directionality (positive downward) as ice-ocean heat flux, and they represent the "maximum" heat flux that the ice can extract. Figures 13 and 14 show the heat content of MLD and melting potential for Exp-CFSD and Exp-PFSD in March and September. As shown in Fig. 13-14, Exp-PFSD shows less melting potential (0-5m) and the heat content within MLD under ice-covered areas compared to Exp-CFSD. This feature is more pronounced in September than in March. Also, heat content in MLD near the ice edge of Exp-PFSD reduces more than other ice-covered areas compared to that of Exp-CFSD, suggesting the role of ice-ocean heat flux. Figures 13 and 14 further support the constraint role of limited oceanic energy to ice melting with respect to varied floe size not only in the surface layer (i.e., melting potential) but also in the mixed layer.

Our fully-coupled simulations also show that atmospheric states respond to changing ice distributions and then modify the energy budget at the ice surface that determines top melt in summer and basal growth in winter. The FSD-varied experiments, in general, show more energy loss from ice to the atmosphere in winter, and all experiments show year-to-year variations of energy gain for sea ice in summer.

The depletion of ocean energy in the surface layer as well as enhanced frazil ice formation are the direct responses to the changes of ice-ocean coupling with the prognostic FSD. The fractured sea ice enlarges the ice-ocean heat flux while the freezing temperature is still determined by the sea surface salinity in the ocean model. However, the local salinity at the ice-ocean interface can be significantly lower than sea surface salinity, and thus higher freezing temperature locally due to the meltwater from sea ice (e.g., the false-bottom, Notz et al., 2003). Schmidt et al. (2004) proposed the ice-ocean heat flux formulation that considers the local salinity equilibrium but its formulation is only for the ice-bottom interface. The generalization of ice-ocean heat flux with the consideration of local salinity equilibrium for both bottom and lateral interface might yield a more realistic ice-ocean coupled simulation. Although the lateral melting rate formulation does not have a major effect on the simulated floe size distribution, the simulated sea ice area and ice mass budget are sensitive to the choice of the formulation. The lateral melting rate formulations applied in this study as well as previous laboratory results are not related to the ice properties (i.e., ice thickness and floe size, Josberger and Martin, 1981; Maykut and Perovich, 1987; Perovich, 1983). A recent laboratory study suggested that the lateral melting rate is a function of temperature difference and the ratio of floe size to ice thickness (Li et al., 2021). Smith et al. (2022) also suggested that Arctic sea ice simulation can be sensitive to the lateral melting rate of Perovich (1983) with different weights on each ice thickness category. Further studies are required to investigate improved lateral melting rate parameterization with observational constraints (e.g., data from the MOSAiC campaign in 2020, Nicolaus et al., 2021) within the prognostic FSD framework.

As discussed in Horvat and Tziperman (2015), the FTSD is sensitive to the wave attenuation coefficients. Our simulations also show substantially contrasting behaviors in the simulated floe size distribution associated with simulated wave parameters, suggesting that several aspects need further investigation. First, the empirical wave attenuation (i.e., IC4M2) may have reasonable performance in simulating the changes of wave energy spectrum locally with specific ice conditions (e.g., Liu et al., 2020). However, the dissipation of wave energy varies spatially for the pan-Arctic (as well as pan-Antarctic) scale simulation with the different sea ice properties (i.e., ice concentration, ice thickness, floe size). Thus, a viscous boundary layer model (Liu et al., 1991) or a viscoelastic model (Wang and Shen, 2010) for wave attenuation, which provides spatially-varied wave attenuation with respect to sea ice properties, might be able to give more realistic simulations in the wave-fracturing process and thus the floe size distribution. Also, the current implementation of sea ice effects in the SWAN model does not include the reflection and scattering due to sea ice, which redistributes the wave energy spatially and potentially changes the wave-fracturing behavior. Second, the probability of floe-fracturing $Q(r)$ in both formulations applied in this study are uncertain. Both formulations result in floe-fracturing into smaller floe size categories within a short time interval as long as the simulated wave parameters satisfy the yielding strain. This strong contribution in the wave-fracturing term is not easily balanced by the floe-welding term. The floe-welding term (Roach et al., 2018a, b) acts to reduce the floe number density so that it is less effective in increasing the representative floe radius if the floe is mostly fractured with the smallest floe size. Third, the attenuated wave energy by sea ice does not influence sea ice conditions in this study. As suggested by Longuet-Higgins and Steward (1962), the attenuated wave energy is transferred into the ocean (as we described in section 3 for wave-enhanced mixing) or sea ice. For sea ice, the transferred energy acts as a stress, called wave radiation stress (WRS), pushing sea ice to the direction of wave propagation. By including the WRS in the momentum equation of ice, the WRS then can affect sea ice drift (e.g., Boutin et al., 2020).

For quantitative applications (e.g., forecasting sea ice), more observations (especially ocean waves under sea ice and FSD) are needed to reduce uncertainties in the atmosphere-ocean-wave-sea ice coupled model, particularly wave-related processes in ice-covered regions. Horvat et al. (2019) developed a new technique to retrieve pan-Arctic scale FSD climatology and seasonal cycle from CryoSat-2 radar altimeter and this method can resolve floe size from 300 m to 100 km and potentially up to 20 m scale if applied to ICESat-2 data. ICESat-2 altimetry also provides a new opportunity to observe ocean waves in sea ice at hemispheric-scale coverage by directly observing the vertical displacements of the ice surface (e.g., Horvat et al., 2020). In situ observations, despite their limited spatial coverage, are valuable wave spectra measurements for wave-physics validation and improvement (e.g., Cooper et al., 2022; Liu et al., 2020).

Code and data availability: The outputs of pan-Arctic simulations analyzed in this study are archived at https://doi.org/10.5281/zenodo.7922725.

Author contributions: CYY and JL designed the model experiments, developed the updated CAPS model, and wrote the manuscript, CYY conducted the experiments and analyzed the results. DC provided constructive feedback on the manuscript.

Competing interests: The authors declare that they have no conflict of interest.

Acknowledgements: This research is supported by the National Natural Science Foundation of China (42006188, 42376237), the National Key R&D Program of China (2018YFA0605901), and the Innovation Group Project of Southern Marine Science and Engineering Guangdong Laboratory (Zhuhai) (311021008). The authors thank the editor, Xichen Li, and two anonymous reviewers for their helpful and constructive comments on the manuscript.

6. References

Asplin, M. G., Scharien, R., Else, B., Howell, S., Barber, D. G., Papakyriakou, T., and Prinsenberg, S.: Implications of fractured Arctic perennial ice cover on thermodynamic and dynamic sea ice processes, J. Geophys. Res. Oceans, 119, 2327–2343, https://doi.org/10.1002/2013JC009557, 2014.

Bai, Q., and Bai, Y.: 7 - Hydrodynamics around Pipes, Subsea Pipeline Design, Analysis, and Installation, Gulf Professional Publishing, 153-170, https://doi.org/10.1016/B978-0-12-386888-6.00007-9, 2014.

Bateson, A. W., Feltham, D. L., Schröder, D., Hosekova, L., Ridley, J. K., and Aksenov, Y.: Impact of sea ice floe size distribution on seasonal fragmentation and melt of Arctic sea ice, The Cryosphere, 14, 403–428, https://doi.org/10.5194/tc-14-403-2020, 2020.

Bateson, A. W., Feltham, D. L., Schröder, D., Wang, Y., Hwang, B., Ridley, J. K., and Aksenov, Y.: Sea ice floe size: its impact on pan-Arctic and local ice mass and required model complexity, The Cryosphere, 16, 2565–2593, https://doi.org/10.5194/tc-16-2565-2022, 2022.

Battjes, J. A. and Janssen, J. P. F. M.: Energy loss and set-up due to breaking of random waves, Proc. 16th Int. Conf. Coastal Engineering, ASCE, 569-587, https://doi.org/10.1061/9780872621909.034, 1978.

Bennetts, L. G., O'Farrell, S., and Uotila, P.: Brief communication: Impacts of ocean-wave-induced breakup of Antarctic sea ice via thermodynamics in a stand-alone version of the CICE sea-ice model, The Cryosphere, 11, 1035–1040, https://doi.org/10.5194/tc-11-1035-2017, 2017.

Bitz, C. M. and Lipscomb, W. H.: An energy-conserving thermodynamic sea ice model for climate study. J. Geophys. Res.-Oceans, 104, 15669–15677, https://doi.org/10.1029/1999JC900100, 1999.

Blanchard-Wrigglesworth, E., Donohoe, A., Roach, L. A., DuVivier, A., and Bitz, C. M.:. High-frequency sea ice variability in observations and models. Geophysical Research Letters, 48, e2020GL092356. https://doi.org/10.1029/2020GL092356, 2021.

Booij, N., Ris, R. C., and Holthuijsen, L. H.: A third-generation wave model for coastal regions. Part I: Model description and validation. Journal of Geophysical Research 104 (C4), 7649–7666, https://doi.org/10.1029/98JC02622, 1999.

Boutin, G., Lique, C., Ardhuin, F., Rousset, C., Talandier, C., Accensi, M., and Girard-Ardhuin, F.: Towards a coupled model to investigate wave–sea ice interactions in the Arctic marginal ice zone, The Cryosphere, 14, 709–735, https://doi.org/10.5194/tc-14-709-2020, 2020.

Bretschneider, C. L.: Wave variability and wave spectra for wind-generated gravity waves, 1959.

Briegleb, B. P. and Light, B.: A Delta-Eddington multiple scattering parameterization for solar radiation in the sea ice component of the Community Climate System Model. (No. NCAR/TN-472+STR). University Corporation for Atmospheric Research, https://doi.org/10.5065/D6B27S71, 2007.

Casas-Prat, M., and Wang, X.: Sea ice retreat contributes to projected increases in extreme Arctic ocean surface waves. Geophysical Research Letters, 47, e2020GL088100. https://doi.org/10.1029/2020GL088100, 2020.

Cassano, J. J., Higgins, M. E., and Seefeldt, M. W.: Performance of the Weather Research and Forecasting Model for Month-Long Pan-Arctic Simulations. Monthly Weather Review, 139, 11, 3469-3488, https://doi.org/10.1175/MWR-D-10-05065.1, 2011.

Cavalieri, D. J., Parkinson, C. L., Gloersen, P., and Zwally, H. J.: updated yearly. Sea Ice Concentrations from Nimbus-7 SMMR and DMSP SSM/I-SSMIS Passive Microwave Data, Version 1. Boulder, Colorado USA. NASA National Snow and Ice Data Center Distributed Active Archive Center. https://doi.org/10.5067/8GQ8LZQVL0VL, 1996.

Chen, F. and Dudhia, J.: Coupling an advanced land surface–hydrology model with the Penn State–NCAR MM5 modeling system. Part I: Model implementation and sensitivity. Mon. Wea. Rev., 129, 569–585, https://doi.org/10.1175/1520-0493(2001)129<0569:CAALSH>2.0.CO;2, 2001.

Cole, S. T., Toole, J. M., Lele, R., Timmermans, M.-L., Gallagher, S. G., Stanton, T. P., Shaw, W. J., Hwang, B., Maksym, T., Wilkinson, J. P., Ortiz, M., Graber, H., Rainville, L., Petty, A. A., Farrell, S. L., Richter-Menge, J. A., and Haas, C.: Ice and ocean velocity in the Arctic marginal ice zone: Ice roughness and momentum transfer, Elementa: Science of the Anthropocene, 5, 55, https://doi.org/10.1525/elementa.241, 2017.

Collins, C. O., III, Rogers, W. E., Marchenko, A., and Babanin, A. V.: In situ measurements of an energetic wave event in the Arctic marginal ice zone, Geophys. Res. Lett., 42, 1863–1870, https://doi.org/10.1002/2015GL063063, 2015.

Collins, C. O., and Rogers, W. E.: A Source Term for Wave Attenuation by Sea ice in WAVEWATCH III: IC4, NRL Report NRL/MR/7320–17-9726, 25pp. Available from https://www7320.nrlssc.navy.mil/pubs.php, 2017.

Collins, W. D., Rasch, P. J., Boville, B. A., McCaa, J., Williamson, D. L., Kiehl, J. T., Briegleb, B. P., Bitz, C., Lin, S.-J., Zhang, M., and Dai, Y.: Description of the NCAR Community Atmosphere Model (CAM 3.0). (No. NCAR/TN-464+STR). University Corporation for Atmospheric Research. https://doi.org/10.5065/D63N21CH, 2004.

Cooper, V. T., Roach, L. A., Thomson, J., Brenner, S. D., Smith, M. M., Meylan, M. H., and Bitz, C.M.: Wind waves in sea ice of the western Arctic and a global coupled wave-ice model. Phil. Trans. R. Soc. A., 380, 20210258, https://doi.org/10.1098/rsta.2021.0258, 2022.

Courtois, P., Hu, X., Pennelly, C., Spence, P., and Myers, P. G.: Mixed layer depth calculation in deep convection regions in ocean numerical models, Ocean Modelling, 120, 67-78, http://dx.doi.org/10.1016/j.ocemod.2017.10.007, 2017.

Curry, J. A., Schramm, J. L., and Ebert, E. E.: Sea ice-albedo climate feedback mechanism, J. Climate, 8, 240–247, https://doi.org/10.1175/1520-0442(1995)008<0240:SIACFM>2.0.CO;2, 1995.

Dobrynin, M., Murawsky, J., and Yang, S.: Evolution of the global wind wave climate in CMIP5 experiments, Geophys. Res. Lett., 39, L18606, https://doi.org/10.1029/2012GL052843, 2012.

Dumont, D., Kohout, A., and Bertino, L.: A wave-based model for the marginal ice zone including a floe breaking parameterization, J. Geophys. Res., 116, C04001, https://doi.org/10.1029/2010JC006682, 2011.

Freitas, S. R., Grell, G. A., Molod, A., Thompson, M. A., Putman, W. M., Santos e Silva, C. M. and Souza, E. P.: Assessing the Grell–Freitas convection parameterization in the NASA GEOS modeling system. J. Adv. Model. Earth Syst., 10, 1266–1289, https://doi.org/10.1029/2017MS001251, 2018.

Gupta, M., and Thompson, A. F.: Regimes of sea-ice floe melt: Ice-ocean coupling at the submesoscales. Journal of Geophysical Research: Oceans, 127, e2022JC018894. https://doi.org/10.1029/2022JC018894, 2022.

Hasselmann, S., Hasselmann, K., Allender, J. H., and Barnett, T. P.: Computations and parameterizations of the nonlinear energy transfer in a gravity wave spectrum. Part II: Parameterizations of the nonlinear transfer for application in wave models, J. Phys. Oceanogr., 15, 11, 1378-1391, https://doi.org/10.1175/1520-0485(1985)015<1378:CAPOTN>2.0.CO;2, 1985.

Horvat, C.: Marginal ice zone fraction benchmarks sea ice climate model skill, Nature communications, 12, 2221, https://doi.org/10.1038/s41467-021-22004-7, 2021.

Horvat, C., Blanchard-Wrigglesworth, E., and Petty, A. A.: Observing waves in sea ice with ICESat-2. Geophysical Research Letters, 47, e2020GL087629. https://doi.org/10.1029/2020GL087629, 2020.

Horvat, C. and Tziperman, E.: A prognostic model of the sea-ice floe size and thickness distribution, The Cryosphere, 9, 2119–2134, https://doi.org/10.5194/tc-9-2119-2015, 2015.

Horvat, C., Tziperman, E., and Campin, J.-M.: Interaction of sea ice floe size, ocean eddies, and sea ice melting, Geophys. Res. Lett., 43, 8083-8090, https://doi.org/10.1002/2016GL069742, 2016.

Horvat, C., Roach, L. A., Tilling, R., Bitz, C. M., Fox-Kemper, B., Guider, C., Hill, K., Ridout, A., and Shepherd, A.: Estimating the sea ice floe size distribution using satellite altimetry: theory, climatology, and model comparison, The Cryosphere, 13, 2869-2885, https://doi.org/10.5194/tc-13-2869-2019, 2019.

Hunke, E. C. and Dukowicz, J. K.: An elastic-viscous-plastic model for sea ice dynamics. J. Phys. Oceanogr. 27, 1849–67, https://doi.org/10.1175/1520-0485(1997)027<1849:AEVPMF>2.0.CO;2, 1997.

Josberger, E. G., and Martin, S.: A laboratory and theoretical study of the boundary layer adjacent to a vertical melting ice wall in salt water. J. Fluid Mech., 111, 439-473, https://doi.org/10.1017/S0022112081002450, 1981.

Kirby, J. T., and Chen, T. M.: Surface waves on vertically sheared flows: approximate dispersion relations. J. Geophys. Res., 94, 1013-1027, https://doi.org/10.1029/JC094iC01p01013, 1989.

Kohout, A., Williams, M. J., Dean, S. M., and Meylan, M.: Storm-induced sea-ice breakup and the implications for ice extent. Nature, 509(7502), 604-607. https://doi.org/10.1038/nature13262, 2014.

Komen, G. J., Hasselmann, S., and Hasselmann, K.: On the existence of a fully developed wind-sea spectrum, J. Phys. Oceanogr., 14, 1271-1285, https://doi.org/10.1175/1520-0485(1984)014<1271:OTEOAF>2.0.CO;2, 1984,

Kumar, N., Voulgaris, G., Warner, J. C., and Olabarrieta, M.: Implementation of the vortex force formalism in the coupled ocean-atmosphere-wave-sediment transport (COAWST) modeling system for inner shelf and surf zone applications, Ocean Modelling, 47, 65-95, https://doi.org/10.1016/j.ocemod.2012.01.003, 2012.

Kwok, R.: Arctic sea ice thickness, volume, and multiyear ice coverage: Losses and coupled variability (1958–2018), Environ. Res. Lett., 13, 105005, https://doi.org/10.1088/1748-9326/aae3ec, 2018.

Langhorne, P. J., Squire, V. A., Fox, C., and Haskell, T. G.: Break-up of sea ice by ocean waves, Annals of Glaciology, 27, 438–442. https://doi.org/10.3189/S0260305500017869, 1998.

Leonard, B., and Mokhtari, S.: ULTRA-SHARP Non oscillatory Convection Schemes for High-Speed Steady Multidimensional Flow. Technical Report. NASA, 1990.

Li, Z., Wang, Z., Wang, Q., Xie, Fei., and Lu, P.: Laboratory study on parameterization of ice floe melt rate at ice-air and ice-water interfaces. Haiyang Xuebao, 43(7), 162-172, https://doi.org/10.12284/hyxb2021115, 2021. (in Chinese)

Liang, X., Losch, M., Nerger, L., Mu, L., Yang, Q., and Liu, C.: Using sea surface temperature observations to constrain upper ocean properties in an Arctic sea ice-ocean data assimilation system, Journal of Geophysical Research: Oceans, 124. https://doi.org/10.1029/2019JC015073, 2019.

Lipscomb, W. H., Hunke, E. C., Maslowski, W., and Jakacki. J.: Ridging, strength, and stability in high-resolution sea ice models. J. Geophys. Res., 112, C03S91, https://doi.org/10.1029/2005JC003355, 2007.

Liu, Q., Babanin, A. V., Zieger, S., Young, I. R., and Guan, C.: Wind and Wave Climate in the Arctic Ocean as Observed by Altimeters. Journal of Climate 29, 22, 7957-7975, https://doi.org/10.1175/JCLI-D-16-0219.1, 2016.

Longuet-Higgins, M. S. and Stewart, R. W.: Radiation stresses and mass transport in surface gravity waves with application to ‘surf beats’, J. Fluid Mech., 13, 481-504, https://doi.org/10.1017/S0022112062000877, 1962.

Loose, B., McGillis, W. R., Perovich, D., Zappa, C. J., and Schlosser, P.: A parameter model of gas exchange for the seasonal sea ice zone, Ocean Sci., 10, 17-28, https://doi.org/10.5194/os-10-17-2014, 2014.

Liu, A. K., Holt, B., and Vachon, P. W.: Wave propagation in the marginal ice zone: Model predictions and comparisons with buoy and synthetic aperture radar data, J. Geophys. Res., 96(C3), 4605-4621, https://doi.org/10.1029/90JC02267, 1991.

Liu, D., Tsarau, A., Guan, C., and Shen, H. H.: Comparison of ice and wind-wave modules in WAVEWATCH III® in the Barents Sea, Cold Regions Science and Technology, 172, 103008, https://doi.org/10.1016/j.coldregions.2020.103008, 2020.

Lu, P., Li, Z., Cheng, B., and Leppäranta, M.: A parameterization of the ice-ocean drag coefficient, J. Geophys. Res., 116, C07019, https://doi.org/10.1029/2010JC006878, 2011.

Lukovich, J. V., Stroeve, J. C., Crawford, A., Hamilton, L., Tsamados, M., Heorton, H., and Massonnet, F.: Summer Extreme Cyclone Impacts on Arctic Sea Ice, Journal of Climate, 34(12), 4817-4834, https://doi.org/10.1175/JCLI-D-19-0925.1, 2021.

Madsen, O. S., Poon, Y.-K., and Graber, H. C.: Spectral wave attenuation by bottom friction: Theory, Proc. 21th Int. Conf. Coastal Engineering, ASCE, 492-504, https://doi.org/10.1061/9780872626874.035, 1988.

Martin, T., Tsamados, M., Schroeder, D., and Feltham, D. L.: The impact of variable sea ice roughness on changes in Arctic Ocean surface stress: A model study, J. Geophys. Res. Oceans, 121, 1931– 1952, https://doi.org/10.1002/2015JC011186, 2016.

Maykut, G. A. and Perovich, D. K.: The role of shortwave radiation in the summer decay of a sea ice cover, J. Geophys. Res.-Ocean., 92, 7032–7044, https://doi.org/10.1029/JC092iC07p07032, 1987.

Maykut, G. A. and McPhee. M. G.: Solar heating of the Arctic mixed layer, J. Geophys. Res.-Oceans, 100, 24691–24703, http://doi.org/10.1029/95JC02554, 1995.

Meylan, M., and Squire, V. A.: The response of ice floes to ocean waves, J. Geophys. Res., 99(C1), 891– 900, https://doi.org/10.1029/93JC02695, 1994.

Meylan, M. H., Bennetts, L. G., and A. L. Kohout: In situ measurements and analysis of ocean waves in the Antarctic marginal ice zone, Geophys. Res. Lett., 41, 1-6, https://doi.org/10.1002/2014GL060809, 2014.

Montiel, F., Squire, V., and Bennetts, L.: Attenuation and directional spreading of ocean wave spectra in the marginal ice zone. Journal of Fluid Mechanics, 790, 492-522. https://doi.org/10.1017/jfm.2016.21, 2016.

Morrison, H., Thompson, G., and Tatarskii, V.: Impact of Cloud Microphysics on the Development of Trailing Stratiform Precipitation in a Simulated Squall Line: Comparison of One– and Two–Moment Schemes. Mon. Wea. Rev., 137, 991-1007. https://doi.org/10.1175/2008MWR2556.1, 2009.

Nakanishi, M., and Niino., H.: Development of an improved turbulence closure model for the atmospheric boundary layer. J. Meteor. Soc. Japan, 87, 895–912, https://doi.org/10.2151/jmsj.87.895, 2009.

Naughten, K. A., Galton-Fenzi, B. K., Meissner, K. J., England, M. H., Brassington, G. B., Colberg, F., Hattermann, T., and Debernard, J. B.: Spurious sea ice formation caused by oscillatory ocean tracer advection schemes. Ocean Model., 116, 108–117, https://doi.org/10.1016/j.ocemod.2017.06.010, 2017.

Nicolaus, M., Perovich, D., Spreen, G., Granskog, M., Albedyll, L., Angelopoulos, M., Anhaus, P., Arndt, S., Belter, H., Bessonov, V., Birnbaum, G., Brauchle, J., Calmer, R., Cardellach, E., Cheng, B., Clemens-Sewall, D., Dadic, R., Damm, E., Boer, G., Demir, O., Dethloff, K., Divine, D., Fong, A., Fons, S., Frey, M., Fuchs, N., Gabarró, C., Gerland, S., Goessling, H., Gradinger, R., Haapala, J., Haas, C., Hamilton, J., Hannula, H.-R., Hendricks, S., Herber, A., Heuzé, C., Hoppmann, M., Høyland, K., Huntemann, M., Hutchings, J., Hwang, B., Itkin, P., Jacobi, H.-W., Jaggi, M., Jutila, A., Kaleschke, L., Katlein, C., Kolabutin, N., Krampe, D., Kristensen, S., Krumpen, T., Kurtz, N., Lampert, A., Lange, B., Lei, R., Light, B., Linhardt, F., Liston, G., Loose, B., Macfarlane, A., Mahmud, M., Matero, I., Maus, S., Morgenstern, A., Naderpour, R., Nandan, V., Niubom, A., Oggier, M., Oppelt, N., Pätzold, F., Perron, C., Petrovsky, T., Pirazzini, R., Polashenski, C., Rabe, B., Raphael, I., Regnery, J., Rex, M., Ricker, R., Riemann-Campe, K., Rinke, A., Rohde, J., Salganik, E., Scharien, R., Schiller, M., Schneebeli, M., Semmling, M., Shimanchuk, E., Shupe, M., Smith, M., Smolyanitsky, V., Sokolov, V., Stanton, T., Stroeve, J., Thielke, L., Timofeeva, A., Tonboe, R., Tavri, A., Tsamados, M., Wagner, D., Watkins, D., Webster, M., and Wendisch, M.: Overview of the MOSAiC expedition – Snow and Sea Ice, Elementa Science of the Anthropocene, https://doi.org/10.1525/elementa.2021.000046, 2021.

Notz, D., McPhee, M. G., Worster, M. G., Maykut, G. A., Schlünzen, K. H., and Eicken, H.: Impact of underwater-ice evolution on Arctic summer sea ice, J. Geophys. Res.-Oceans, 108, 3223, https://doi.org/10.1029/2001JC001173, 2003.

Notz, D., Jahn, A., Holland, M., Hunke, E., Massonnet, F., Stroeve, J., Tremblay, B., and Vancoppenolle, M.: The CMIP6 Sea-Ice Model Intercomparison Project (SIMIP): understanding sea ice through climate-model simulations, Geosci. Model Dev., 9, 3427-3446, https://doi.org/10.5194/gmd-9-3427-2016, 2016.

Parkinson, C. L., and Comiso, J. C.: On the 2012 record low Arctic sea ice cover: Combined impact of preconditioning and an August storm. Geophysical Research Letters, 40, 1356–1361. https://doi.org/10.1002/grl.50349, 2013.

Peng, L., Zhang, X., Kim, J.-H., Cho, K.-H., Kim, B.-M., Wang, Z., and Tang, H.: Role of intense Arctic storm in accelerating summer sea ice melt: An in situ observational study. Geophysical Research Letters, 48, e2021GL092714. https://doi.org/10.1029/2021GL092714, 2021.

Perovich, D.: On the summer decay of a sea ice cover, PhD thesis, University of Washington, Seattle, 48–96, 1983.

Perovich, D., Meier, W., Tshudi, M., Hendricks, S., Petty, A. A., Divine, D., Farrell, S., Gerland, S., Haas, C., Kaleschke, L., Pavlova, O., Ricker, R., Tian-Kunze, X., Webster, M., and

Wood, K.: Sea Ice, Arctic Report Card 2020, Thoman, R. L., Richter-Menge, J., and Druckenmiller, M. L., Eds., https://doi.org/10.25923/n170-9h57, 2020.

Rampal, P., Weiss, J., and Marsan, D.: Positive trend in the mean speed and deformation rate of Arctic sea ice, 1979–2007, J. Geophys. Res., 114, C05013, https://doi.org/10.1029/2008JC005066, 2009.

Roach, L. A., Horvat, C., Dean, S. M., and Bitz, C. M.: An emergent sea ice floe size distribution in a global coupled ocean-sea ice model. Journal of Geophysical Research: Oceans, 123, 4322–4337. https://doi.org/10.1029/2017JC013692, 2018a.

Roach, L. A., Smith, M. M., and Dean, S. M.: Quantifying growth of pancake sea ice floes using images from drifting buoys. Journal of Geophysical Research: Ocean, 123, 2851-2866. https://doi.org/10.1002/2017JC013693, 2018b.

Roach, L. A., Bitz, C. M., Horvat, C., and Dean, S. M.: Advances in Modeling Interactions Between Sea Ice and Ocean Surface Waves, J. Adv. Model. Earth Syst., 11, 4167-4181, https://doi.org/10.1029/2019MS001836, 2019.

Rogers, W. E., Meylan, M. H., and Kohout, A. L.: Frequency Distribution of Dissipation of Energy of Ocean Waves by Sea Ice Using Data from Wave Array 3 of the ONR ”Sea State” Field Experiment. NRL Report NRL/MR/7322–18-9801., 25 pp, Available from https://www7320.nrlssc.navy.mil/pubs.php, 2018.

Rogers, W. E.: Implementation of sea ice in the wave model SWAN, NRL Memorandum Report NRL/MR/7322–19-9874, 25pp, Available from https://www7320.nrlssc.navy.mil/pubs.php, 2019.

Rothrock, D. A. and Thorndike, A. S.: Measuring the sea ice floe size distribution, J. Geophys. Res., 89, 6477–6486, https://doi.org/10.1029/JC089iC04p06477, 1984.

Saha, S., Moorthi, S., Wu, X., Wang, J., Nadiga, S., Tripp, P., Behringer, D., Hou, Y., Chuang, H., Iredell, M., Ek, M., Meng, J., Yang, R., Mendez, M. P., van den Dool, H., Zhang, Q., Wang, W., Chen, M., and Becker, E.: The NCEP climate forecast system version 2, J. Climate, 27, 2185–2208, https://doi.org/10.1175/JCLI-D-12-00823.1, 2014.

Schäfer, M., Bierwirth, E., Ehrlich, A., Jäkel, E., and Wendisch, M.: Airborne observations and simulations of three-dimensional radiative interactions between Arctic boundary layer clouds and ice floes, Atmos. Chem. Phys., 15, 8147-8163, https://doi.org/10.5194/acp-15-8147-2015, 2015.

Schmidt, G. A., Bitz, C. M., Mikolajewicz, U., and Tremblay, L.-B.: Ice–ocean boundary conditions for coupled models, Ocean Model., 7, 59-74, https://doi.org/10.1016/S1463-5003(03)00030-1, 2004.

Sepp, M., and Jaagus, J.: Changes in the activity and tracks of Arctic cyclones. Climatic Change, 105(3), 577–595. https://doi.org/10.1007/s10584-010-9893-7, 2011.

Shchepetkin, A. F., and McWilliams, J. C.: The Regional Ocean Modeling System: A split-explicit, free-surface, topography following coordinates ocean model, Ocean Modelling, 9, 347-404, https://doi.org/10.1016/j.ocemod.2004.08.002, 2005.

Simmonds, I., and Rudeva, I.: The great Arctic cyclone of August 2012, Geophys. Res. Lett., 39, L23709, https://doi.org/10.1029/2012GL054259, 2012.

Smith, M. M., Holland, M., and Light, B.: Arctic sea ice sensitivity to lateral melting representation in a coupled climate model, The Cryosphere, 16, 419-434, https://doi.org/10.5194/tc-16-419-2022, 2022.

Spreen, G., Kwok, R., and Menemenlis, D.: Trends in Arctic sea ice drift and role of wind forcing: 1992–2009, Geophys. Res. Lett., 38, L19501, https://doi.org/10.1029/2011GL048970, 2011.

Squire, V. A.: Ocean Wave Interactions with Sea Ice: A Reappraisal, Annual Review of Fluid Mechanics, 52:1, 37-60, https://doi.org/10.1146/annurev-fluid-010719-060301, 2020.

Squire, V. A., and Montiel, F.: Evolution of Directional Wave Spectra in the Marginal Ice Zone: A New Model Tested with Legacy Data. Journal of Physical Oceanography 46, 10, 3121-3137, https://doi.org/10.1175/JPO-D-16-0118.1, 2016.

Steele, M.: Sea ice melting and floe geometry in a simple ice-ocean model, J. Geophys. Res., 97, 17-729-17738, https://doi.org/10.1029/92JC01755, 1992.

Steele, M., Morison, J. H., and Untersteiner, N.: The partition of air-ice-ocean momentum exchange as a function of ice concentration, floe size, and draft, J. Geophys. Res., 94(C9), 12739-12750, https://doi.org/10.1029/JC094iC09p12739, 1989.

Steer, A., Worby, A., and Heil, P.: Observed changes in sea-ice floe size distribution during early summer in the western Weddell Sea, Deep Sea Res., Part II, 55, 933-942, https://doi.org/10.1016/j.dsr2.2007.12.016, 2008.

Stern, D., P, Doyle, J. D., Barton, N. P., Finocchio, P. M., Komaromi, W. A., & Metzger, E. J.: The impact of an intense cyclone on short-term sea ice loss in a fully coupled atmosphere-ocean-ice model. Geophysical Research Letters, 47, e2019GL085580. https://doi.org/10.1029/2019GL085580, 2020.

Stopa, J. E., Ardhuin, F., and Girard-Ardhuin, F.: Wave climate in the Arctic 1992-2014: seasonality and trends, The Cryosphere, 10, 1605–1629, https://doi.org/10.5194/tc-10-1605-2016, 2016.

Taylor, P. K., and Yelland, M. J.: The dependence of sea surface roughness on the height and steepness of the waves. Journal of Physical Oceanography 31, 572-590, https://doi.org/10.1175/1520-0485(2001)031<0572:TDOSSR>2.0.CO;2, 2001.

Thomson, J., and Rogers, W. E.: Swell and sea in the emerging Arctic Ocean, Geophys. Res. Lett., 41, 3136–3140, https://doi.org/10.1002/2014GL059983, 2014.

Thorndike, A. S., Rothrock, D. A., Maykut, G. A., and Colony, R.: The thickness distribution of sea ice, J. Geophys. Res., 80, 4501, https://doi.org/10.1029/JC080i033p04501, 1975.

Toyota, T., Takatsuji, S., and Nakayama, M.: Characteristics of sea ice floe size distribution in the seasonal ice zone, Geophys. Res. Lett., 33, L02616, https://doi.org/10.1029/2005GL024556, 2006.

Toyota, T., Haas, C., and Tamura, T.: Size distribution and shape properties of relatively small sea-ice floes in the Antarctic marginal ice zone in late winter, Deep Sea Res., Part II, 58, 1182–1193, https://doi.org/10.1016/j.dsr2.2010.10.034, 2011.

Tschudi, M. A., Stroeve, J. C., and Stewart, J. S.: Relating the age of Arctic sea ice to its thickness, as measured during NASA's ICESat and IceBridge campaigns. Remote Sensing, 8(6), 457, 2016.

Tsamados, M., Feltham, D. L., Schroeder, D., Flocco, D., Farrell, S. L., Kurtz, N., Laxon, S. W., and Bacon, S.: Impact of Variable Atmospheric and Oceanic Form Drag on Simulations of Arctic Sea Ice. Journal of Physical Oceanography 44, 5, 1329-1353, https://doi.org/10.1175/JPO-D-13-0215.1, 2014.

Tsamados, M., Feltham, D., Petty, A., Schroeder, D., Flocco. D.: Processes controlling surface, bottom and lateral melt of Arctic sea ice in a state of the art sea ice model. Phil. Trans. R. Soc. A, 373: 20140167. https://doi.org/10.1098/rsta.2014.0167, 2015.

Uchiyama, Y., McWilliams, J. C., and Shchepetkin, A. F.: Wave–current interaction in an oceanic circulation model with a vortex-force formalism: Application to the surf zone, Ocean Modelling, 34, 1-2, 16-35, https://doi.org/10.1016/j.ocemod.2010.04.002, 2010.

Umlauf, L. and Burchard, H.: A generic length-scale equation for geophysical turbulence models, J. Marine Res., 61, 235-265, https://doi.org/10.1357/002224003322005087, 2003.

Valkonen, E., Cassano, J., and Cassano, E.: Arctic cyclones and their interactions with the declining sea ice: A recent climatology. Journal of Geophysical Research: Atmospheres, 126, e2020JD034366. https://doi.org/10.1029/2020JD034366, 2021.

Vella, D., and Wettlaufer, J. S.: Explaining the patterns formed by ice floe interactions, J. Geophys. Res., 113, C11011, https://doi.org/10.1029/2008JC004781, 2008.

Wang, R., and Shen, H. H.: Gravity waves propagating into an ice-covered ocean: A viscoelastic model, J. Geophys. Res., 115, C06024, https://doi.org/10.1029/2009JC005591, 2010.

Warner, J. C., Armstrong, B., He, R., and Zambon, J.: Development of a coupled ocean-atmosphere-wave-sediment transport (COAWST) modeling system. Ocean Modell. 35, 230–244, https://doi.org/10.1016/j.ocemod.2010.07.010, 2010.

Waseda, T., Nose, T., Kodaira, T., Sasmal, K., and Webb, A.: Climatic trends of extreme wave events caused by Arctic cyclones in the western Arctic Ocean. Polar Science, 27, 100625. https://doi.org/10.1016/j.polar.2020.100625, 2021.

Waseda, T., Webb, A., Sato, K., Inoue, J., Kohout, A., Penrose, B., and Penrose, S.: Correlated Increase of High Ocean Waves and Winds in the Ice-Free Waters of the Arctic Ocean. Sci Rep 8, 4489, https://doi.org/10.1038/s41598-018-22500-9, 2018.

Weiss J. and Dansereau V.: Linking scales in sea ice mechanics. Phil. Trans. R. Soc. A., 375, 20150352, http://doi.org/10.1098/rsta.2015.0352, 2017.

Wenta, M., Herman, A.: Area-Averaged Surface Moisture Flux over Fragmented Sea Ice: Floe Size Distribution Effects and the Associated Convection Structure within the Atmospheric Boundary Layer. Atmosphere, 10, 654. https://doi.org/10.3390/atmos10110654, 2019.

Wilchinsky, A. V., Feltham, D. L., and Hopkins, M. A.: Effect of shear rupture on aggregate scale formation in sea ice, J. Geophys. Res., 115, C10002, https://doi.org/10.1029/2009JC006043, 2010.

Yang, C.-Y., Liu, J., and Xu, S.: Seasonal Arctic sea ice prediction using a newly developed fully coupled regional model with the assimilation of satellite sea ice observations, J. Adv. Model. Earth Sy., 12, e2019MS001938, https://doi.org/10.1029/2019MS001938, 2020.

Yang, C.-Y., Liu, J., and Chen, D.: An improved regional coupled modeling system for Arctic sea ice simulation and prediction: a case study for 2018, Geosci. Model Dev., 15, 1155–1176, https://doi.org/10.5194/gmd-15-1155-2022, 2022.

Zahn, M., Akperov, M., Rinke, A., Feser, F., and Mokhov, I. I.: Trends of cyclone characteristics in the Arctic and their patterns from different reanalysis data. Journal of Geophysical Research: Atmospheres, 123, 2737–2751. https://doi.org/10.1002/2017JD027439, 2018.

Zhang, F., Pang, X., Lei, R., Zhai, M., Zhao, X., and Cai, Q.: Arctic sea ice motion change and response to atmospheric forcing between 1979 and 2019. International Journal of Climatology, 42(3), 1854-1876. https://doi.org/10.1002/joc.7340, 2022

Zhang, J., Lindsay, R., Schweiger, A., and Steele, M.: The impact of an intense summer cyclone on 2012 Arctic sea ice retreat. Geophysical Research Letters, 40, 720-726. https://doi.org/10.1002/grl.50190, 2013.

Zhang, J., Schweiger, A., Steele, M., and Stern, H.: Sea ice floe size distribution in the marginal ice zone: Theory and numerical experiments, J. Geophys. Res. Oceans, 120, https://doi.org/10.1002/2015JC010770, 2015.

Zhang, J., Stern, H., Hwang, B., Schweiger, A., Steele, M., Stark, M., Graber, H. C.: Modeling the seasonal evolution of the Arctic sea ice floe size distribution. Elementa: Science of the Anthropocene, 4, 000126, https://doi.org/10.12952/journal.elementa.000126, 2016.

7. Tables

Table 1 The summary of physic parameterizations used in all pan-Arctic simulations.

WRF physics	
Cumulus	Grell-Freitas (Freitas et al. 2018)
Microphysics	Morrison 2-moment (Morrison et al. 2009)
Longwave radiation	CAM spectral band scheme (Collins et al. 2004)
Shortwave radiation	CAM spectral band scheme (Collins et al. 2004)
Boundary layer	MYNN (Nakanishi and Niino, 2009)
Land surface	Unified Noah LSM (Chen and Dudhia, 2001)
ROMS physics	
Tracer advection	Upwind third-order horizontal advection (U3H; Shchepetkin, and McWilliams, 2005) Centered fourth-order vertical advection (C4V; Shchepetkin, and McWilliams, 2005)
Tracer vertical mixing	Generic Length-Scale scheme (Umlauf and Burchard, 2003)
CICE physics	
Ice dynamics	EVP (Hunke and Dukowicz, 1997)
Ice thermodynamics	Bitz and Lipscomb (1999)
Shortwave albedo	Delta-Eddington (Briegleb and Light, 2007)
SWAN physics	
Exponential wind growth	Komen et al. (1984)
Whitecapping	Komen et al. (1984)
Quadruplets	Hasselmann et al. (1985)
Depth-induced breaking	Battjes and Janssen (1978)
Bottom friction	Madsen et al. (1988)
Sea ice dissipation	Collins and Rogers (2017); Rogers (2019)

Table 2 The summary of the experiments conducted in this study and their main changes in the experiment design. MP87: Maykut and Perovich (1987). P83: Perovich (1983). M14: Meylan et al. (2014). R18: Rogers et al. (2018).

Experiment	Floe size	Lateral melting rate	Wave fracturing formulation	Wave attenuation coefficients
Exp-CFSD	Const. 300m	MP87	None	M14
Exp-PFSD	FSTD	MP87	Equally (PF1)	M14
Exp-LatMelt-C	Const. 300m	P83	None	M14
Exp-LatMelt-P	FSTD	P83	Equally (PF1)	M14
Exp-WaveFrac-P	FSTD	MP87	Bretschneider (PF2)	M14
Exp-WaveAtt-C	Const. 300m	MP87	None	R18
Exp-WaveAtt-P	FSTD	MP87	Equally (PF1)	R18

8. Figures

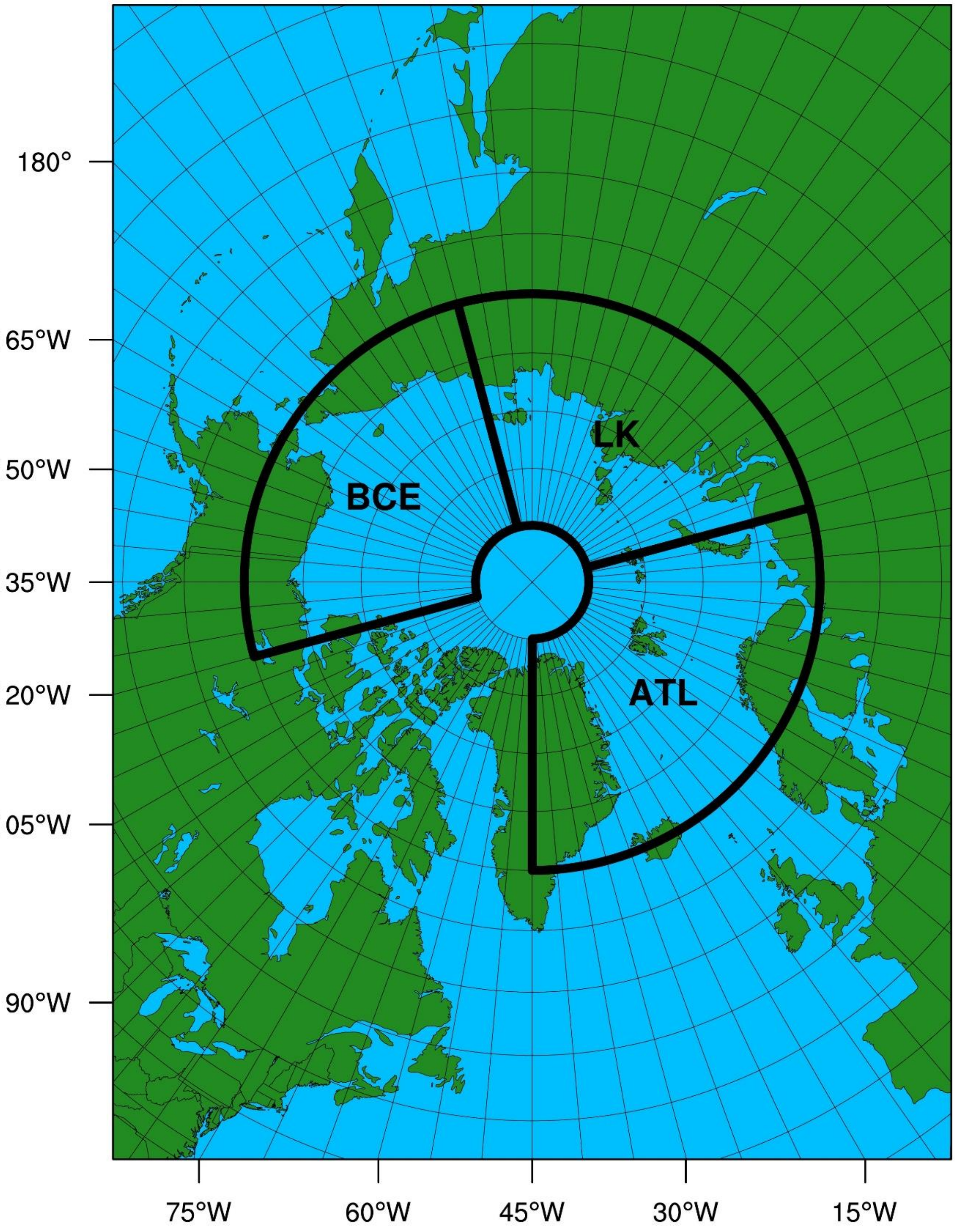

Figure 1 The model domain used in CAPS for pan-Arctic sea ice simulations. Black boxes indicate the subregions for analysis performed in this study.

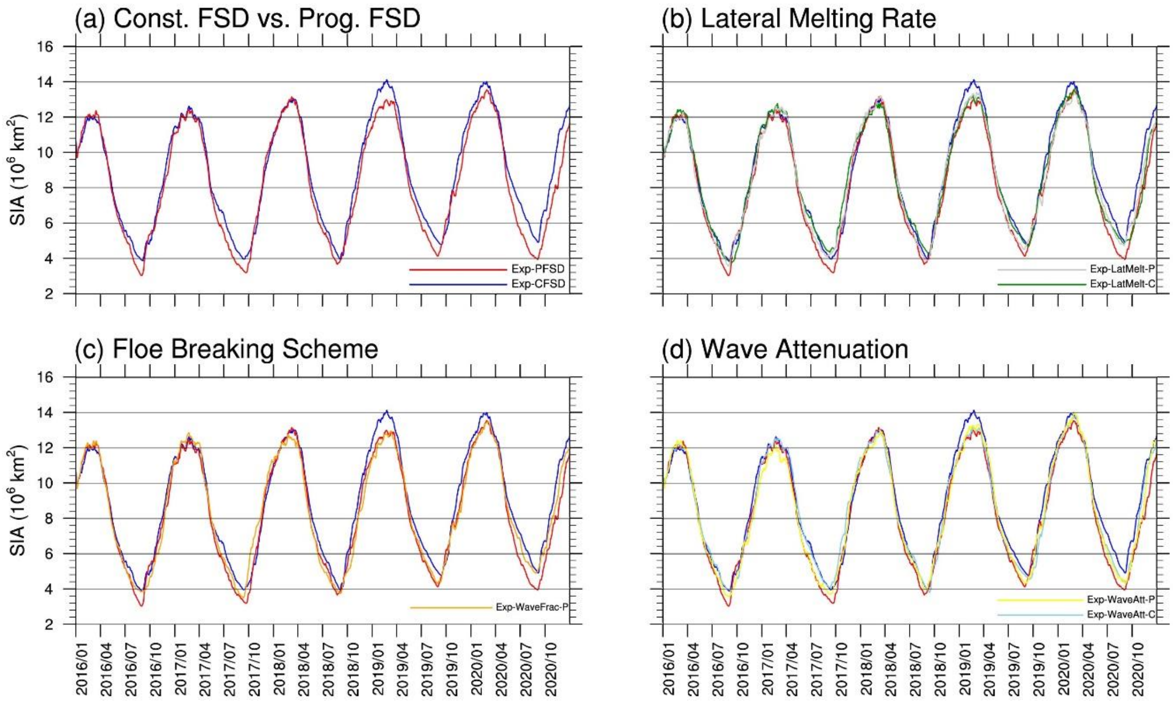

Figure 2 Time-series of Arctic sea ice area for Exp-CFSD (blue line), Exp-PFSD (red line), Exp-LatMelt-C (green line), Exp-LatMelt-P (grey line), Exp-WaveFrac-P (orange line), Exp-WaveAtt-C (light-blue line) and Exp-WaveAtt-P (yellow line).

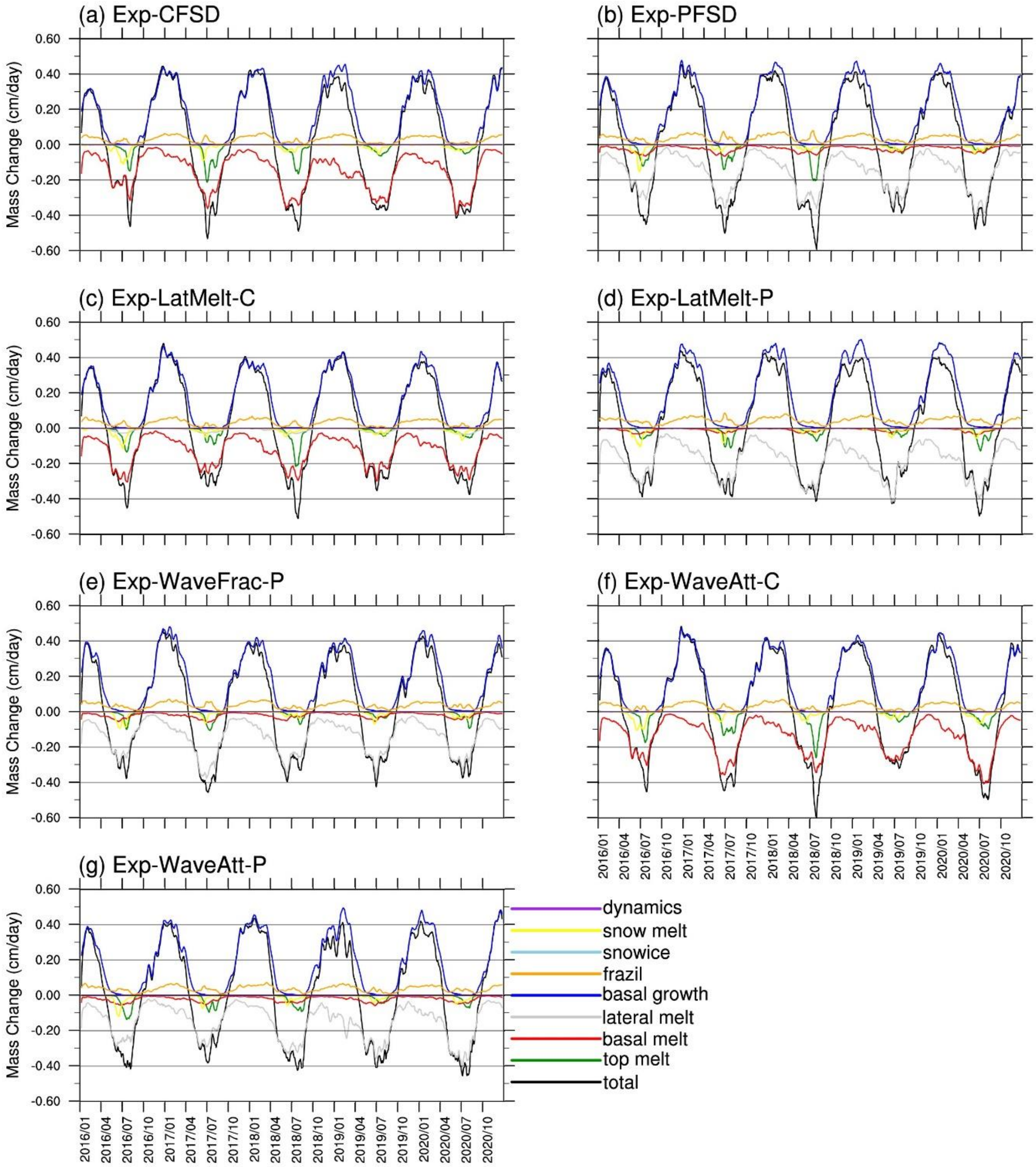

Figure 3 Time-series (15-day running-averaged) of sea ice mass budget terms for (a) Exp-CFSD, (b) Exp-PFSD, (c) Exp-LatMelt-C, (d) Exp-LatMelt-P, (e) Exp-WaveFrac-P, (f) Exp-WaveAtt-C, and (g) Exp-WaveAtt-P. Ice mass budget terms include: total mass change (black line), sea ice melt at the air-ice interface (top melt, green line), sea ice melt at the bottom of the ice (basal melt, red line), sea ice melt at the sides of the ice (lateral melt, grey line), sea ice growth at the bottom of the ice (basal growth, blue line), sea ice growth by supercooled open water (frazil, orange line), sea ice growth due to transformation of snow to sea ice (snowice, light-blue line), and sea ice mass change due to dynamics-related processes (dynamics, purple line) (Notz et al., 2016; Yang et al., 2022). For reference, snow melt term (yellow line) is included.

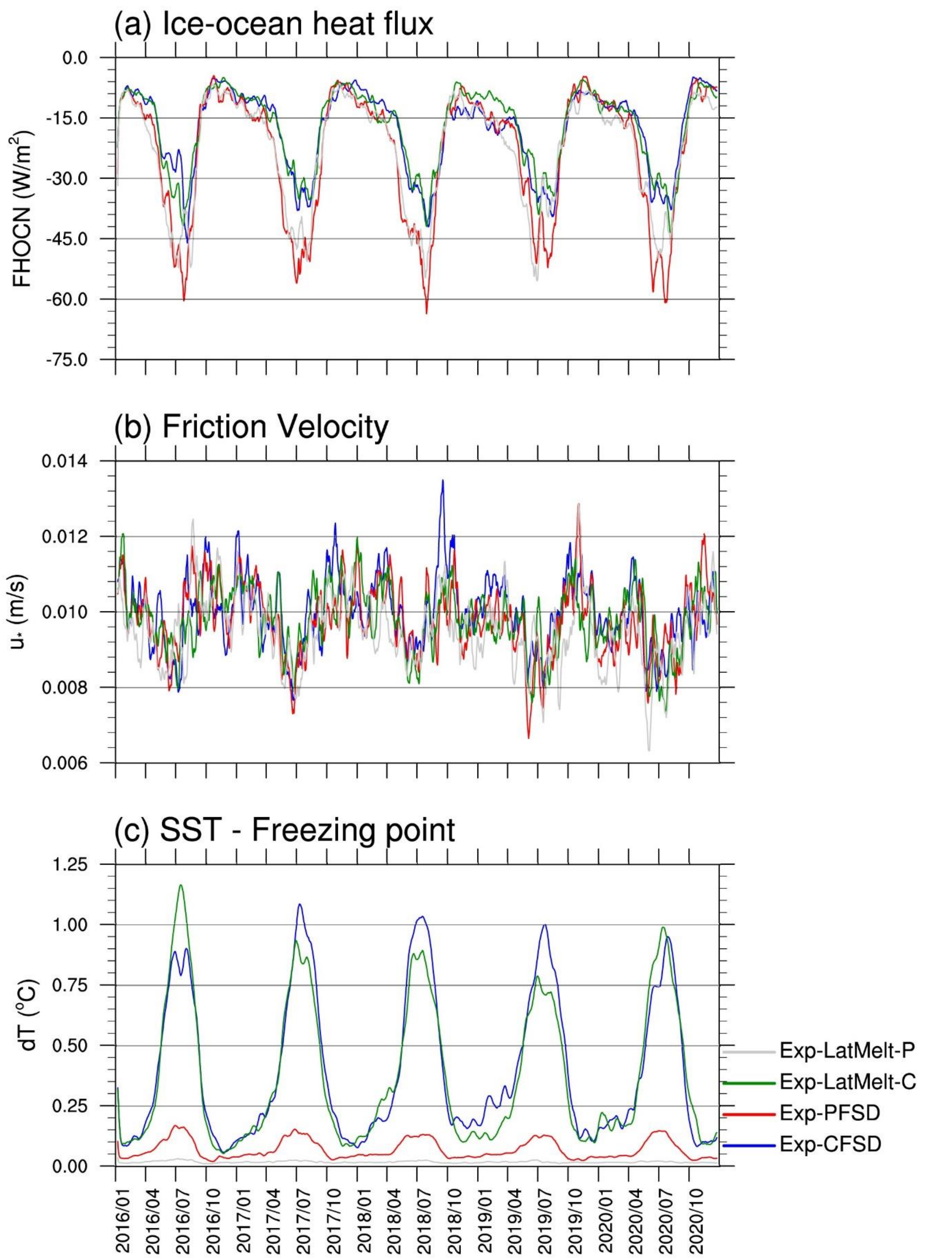

Figure 4 Time-series (15-day running-averaged) of (a) ice-ocean heat flux, (b) friction velocity at ice-ocean interface, and (c) the temperature difference between SST and freezing point for Exp-CFSD (blue line), Exp-PFSD (red line), Exp-LatMelt-C (green line), and Exp-LatMelt-P (grey line). Note: (a) is positive downward and weighted by ice concentration.

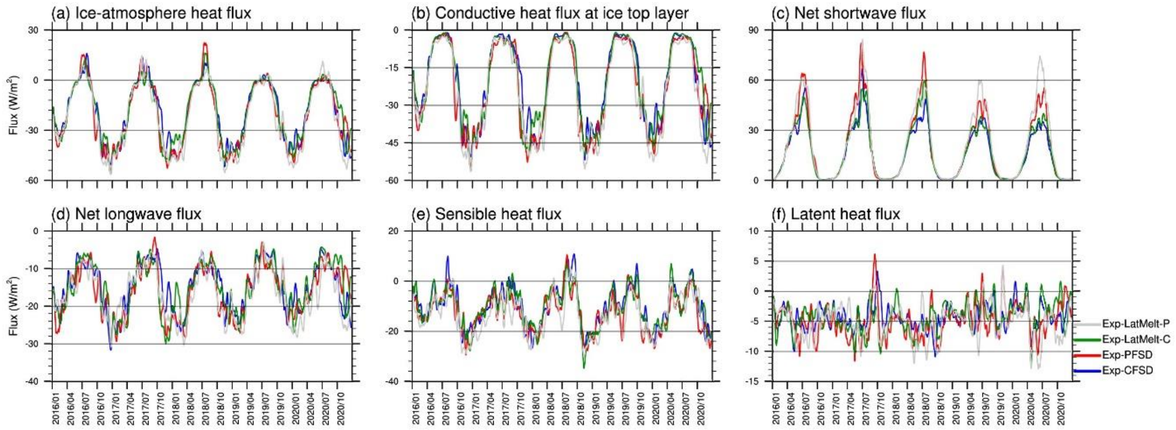

Figure 5 Time-series (15-day running-averaged) of (a) ice-atmosphere heat flux, (b) conductive heat flux at the ice top layer, (c) net shortwave flux, (d) net longwave flux, (e) sensible heat flux, and (f) latent heat flux for Exp-CFSD (blue line), Exp-PFSD (red line), Exp-LatMelt-C (green line), and Exp-LatMelt-P (grey line). Note: (a)-(e) are positive downwards and weighted by ice concentration.

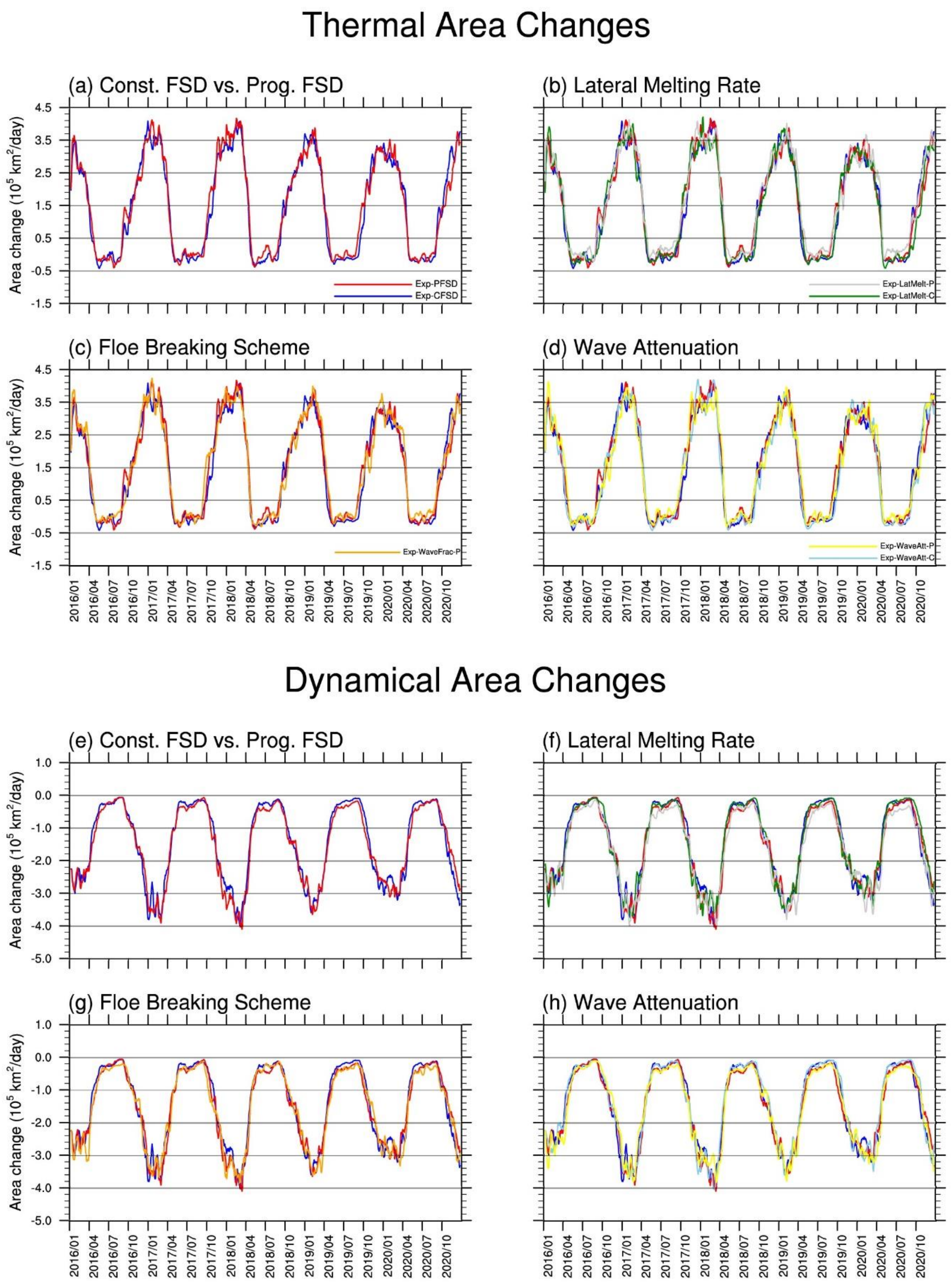

Figure 6 Time-series (15-day running-averaged) of sea ice area changes due to thermal processes (a-d, upper panel) and dynamical processes (e-h, bottom panel) for Exp-CFSD (blue line), Exp-PFSD (red line), Exp-LatMelt-C (green line), Exp-LatMelt-P (grey line), Exp-WaveFrac-P (orange line), Exp-WaveAtt-C (light-blue line) and Exp-WaveAtt-P (yellow line).

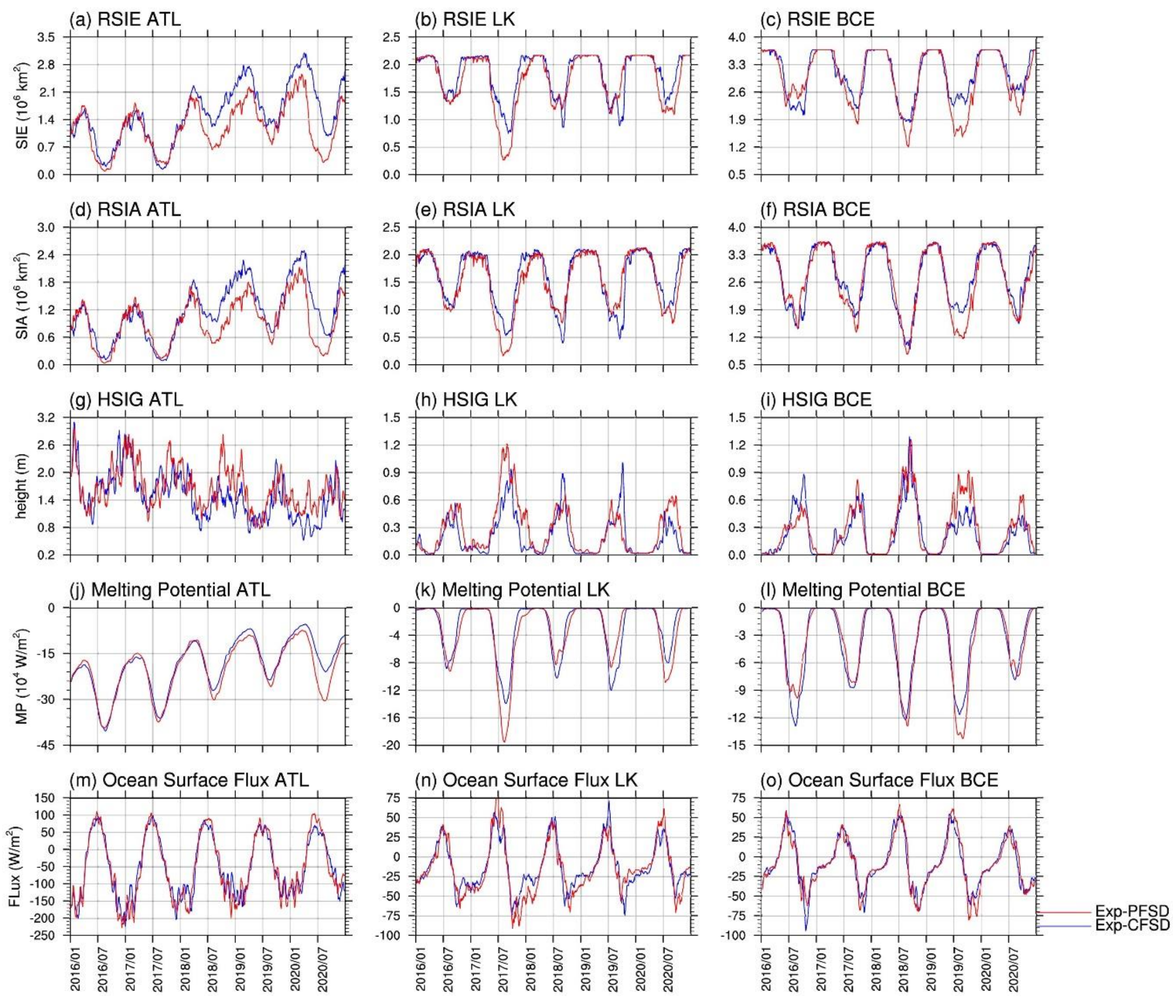

Figure 7 Time-series of (a-c) ice extent, (d-f) ice area, (g-i) significant wave height, (j-l) melting potential, and (m-o) heat flux at the ocean surface in ATL, LK, and BCE regions for Exp-CFSD (blue line) and Exp-PFSD (red line). Note: significant wave height, melting potential, and heat flux at the ocean surface are region-averaged and 15-day running-averaged values.

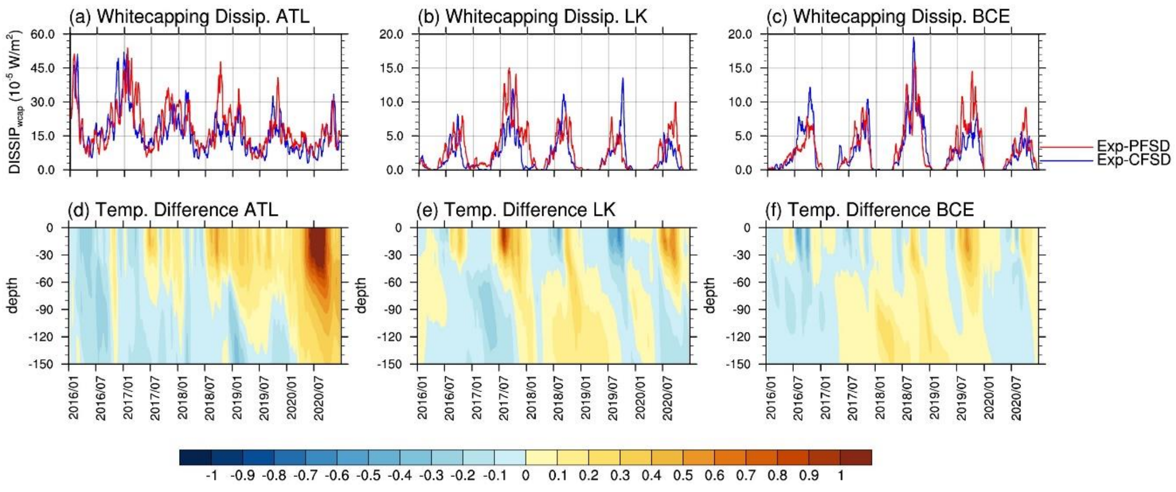

Figure 8 Time-series (15-day running-averaged) of white capping dissipation averaged over (a) ATL, (b) LK, and (c) BCE regions for Exp-CFSD (blue line) and Exp-PFSD (red line), and the temperature profile difference between Exp-CFSD and Exp-PFSD in the upper 150 m averaged over (d) ATL, (e) LK, and (f) BCE regions.

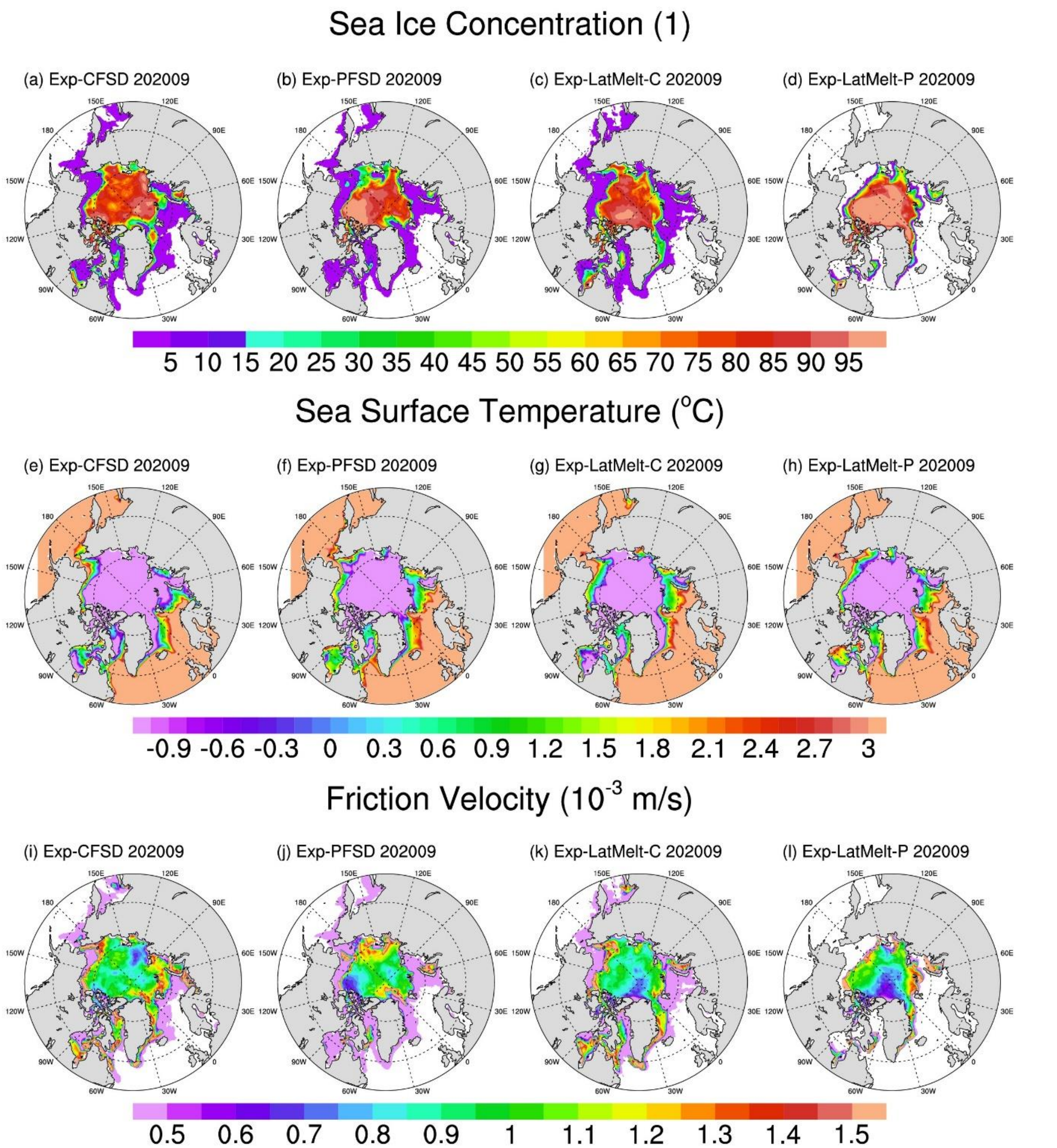

Figure 9 The monthly-mean of (a-d) sea ice concentration, (e-h) sea surface temperature, and (i-l) friction velocity in September 2020 for Exp-CFSD, Exp-PFSD, Exp-LatMelt-C, and Exp-LatMelt-P.

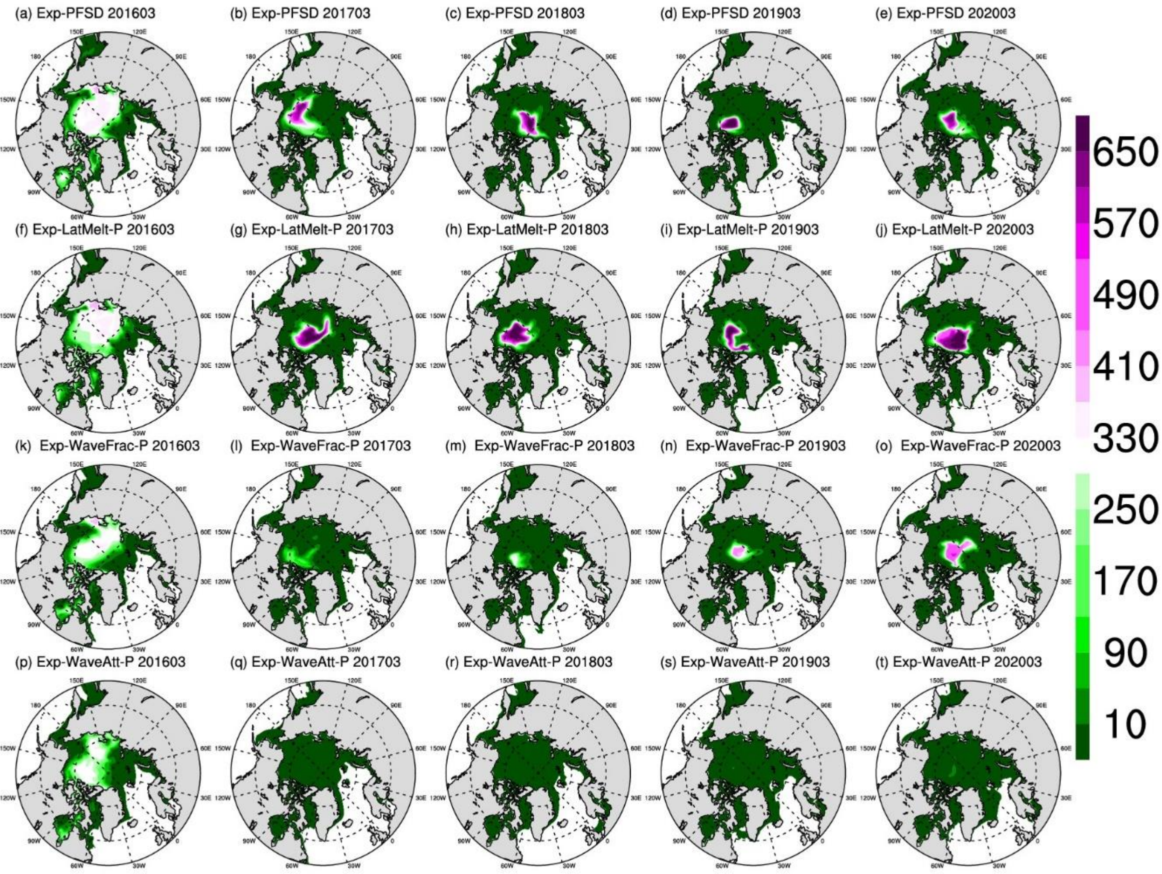
(a) Exp-PFSD 201603
(b) Exp-PFSD 201703
(c) Exp-PFSD 201803
(d) Exp-PFSD 201903
(e) Exp-PFSD 202003
(f) Exp-LatMelt-P 201603
(g) Exp-LatMelt-P 201703
(h) Exp-LatMelt-P 201803
(i) Exp-LatMelt-P 201903
(j) Exp-LatMelt-P 202003
(k) Exp-WaveFrac-P 201603
(l) Exp-WaveFrac-P 201703
(m) Exp-WaveFrac-P 201803
(n) Exp-WaveFrac-P 201903
(o) Exp-WaveFrac-P 202003
(p) Exp-WaveAtt-P 201603
(q) Exp-WaveAtt-P 201703
(r) Exp-WaveAtt-P 201803
(s) Exp-WaveAtt-P 201903
(t) Exp-WaveAtt-P 202003
650
570
490
410
330
250
170
90
10

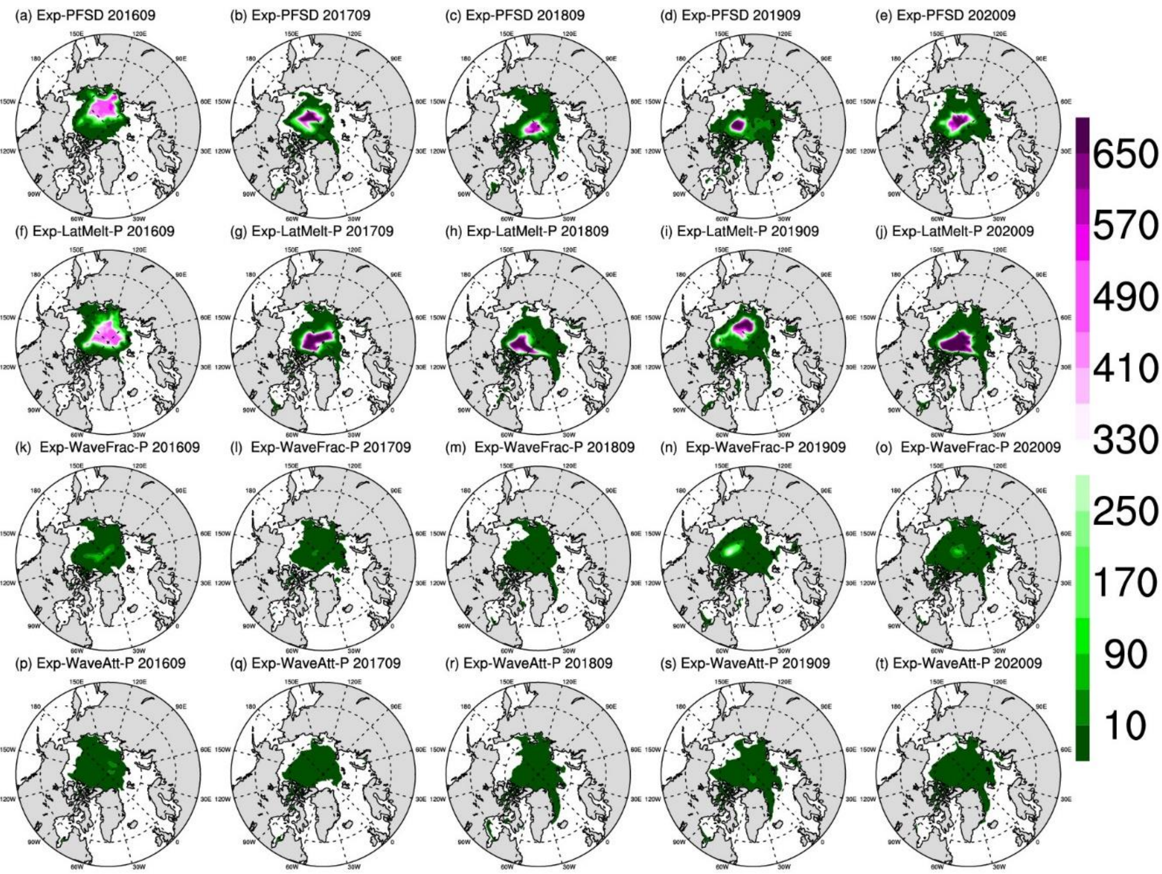
(a) Exp-PFSD 201609
(b) Exp-PFSD 201709
(c) Exp-PFSD 201809
(d) Exp-PFSD 201909
(e) Exp-PFSD 202009
(f) Exp-LatMelt-P 201609
(g) Exp-LatMelt-P 201709
(h) Exp-LatMelt-P 201809
(i) Exp-LatMelt-P 201909
(j) Exp-LatMelt-P 202009
(k) Exp-WaveFrac-P 201609
(l) Exp-WaveFrac-P 201709
(m) Exp-WaveFrac-P 201809
(n) Exp-WaveFrac-P 201909
(o) Exp-WaveFrac-P 202009
(p) Exp-WaveAtt-P 201609
(q) Exp-WaveAtt-P 201709
(r) Exp-WaveAtt-P 201809
(s) Exp-WaveAtt-P 201909
(t) Exp-WaveAtt-P 202009
650
570
490
410
330
250
170
90
10

Figure 10 The spatial distribution of the representative floe radius in March (upper panel) and September (bottom panel) of (a-e) Exp-PFSD, (f-j) Exp-LatMelt-P, (k-o) Exp-WaveFrac-P, and (p-t) Exp-WaveAtt-P for 2016-2020. Note: cells with less than 15% ice concentration are treated as missing values.

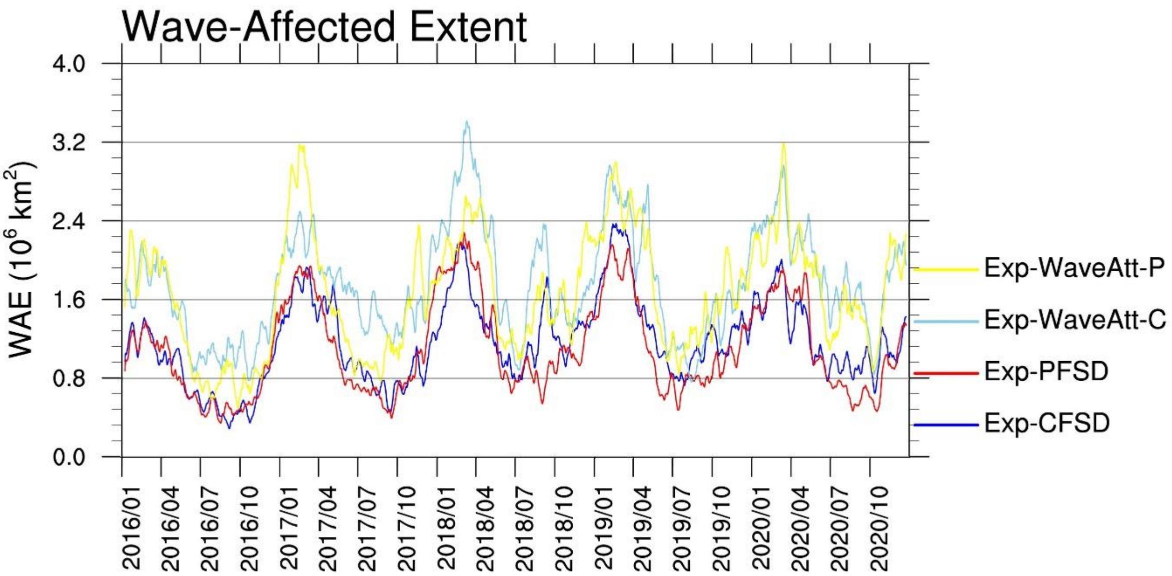

Figure 11 Time-series (15-day running-averaged) of Arctic wave-affected extent for Exp-CFSD (blue line), Exp-PFSD (red line), Exp-WaveAtt-C (light-blue line) and Exp-WaveAtt-P (yellow line).

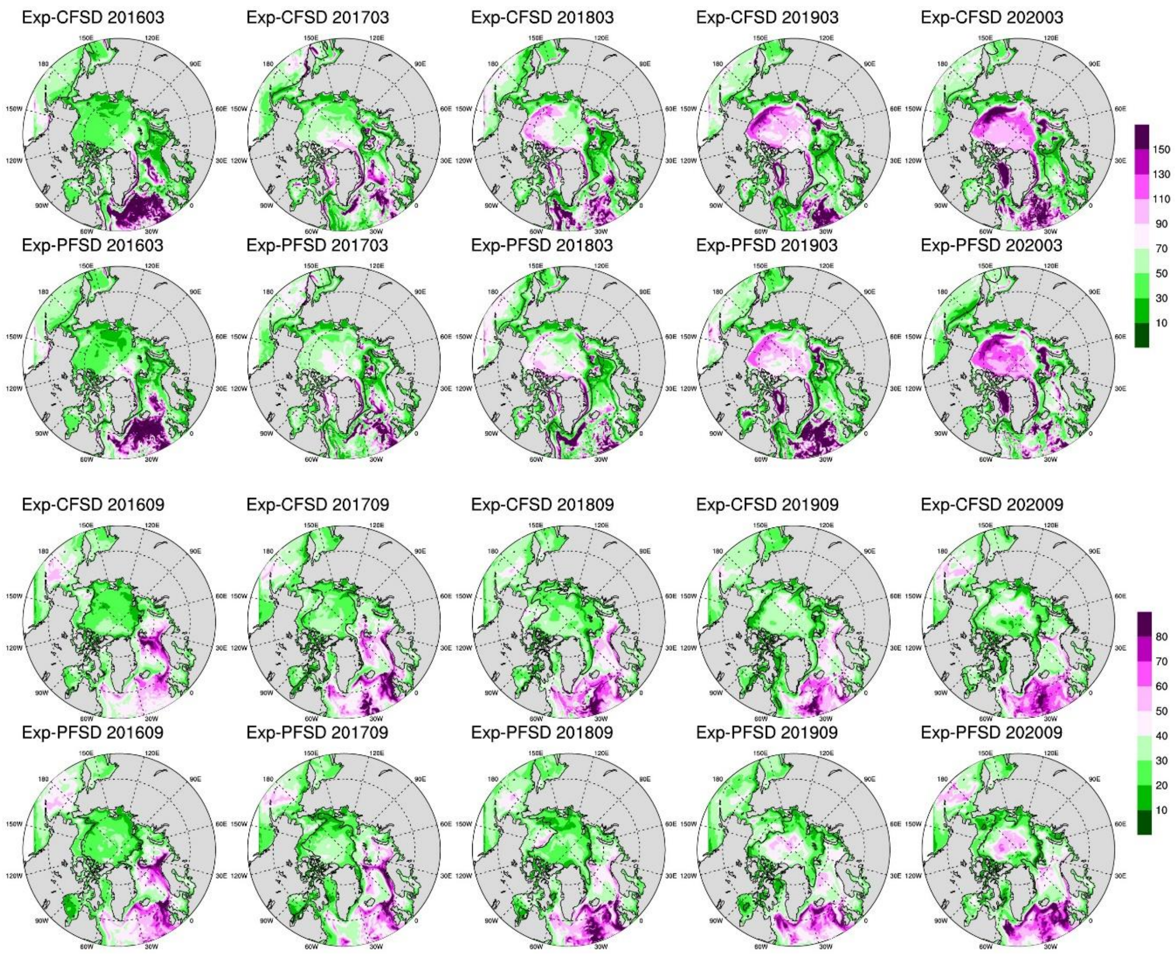

Figure 12 Monthly mean of MLD in March (top panel) and September (bottom panel) of Exp-CFSD and Exp-PFSD for 2016-2020. Note: the black contour represents the average location of 15% ice concentration.

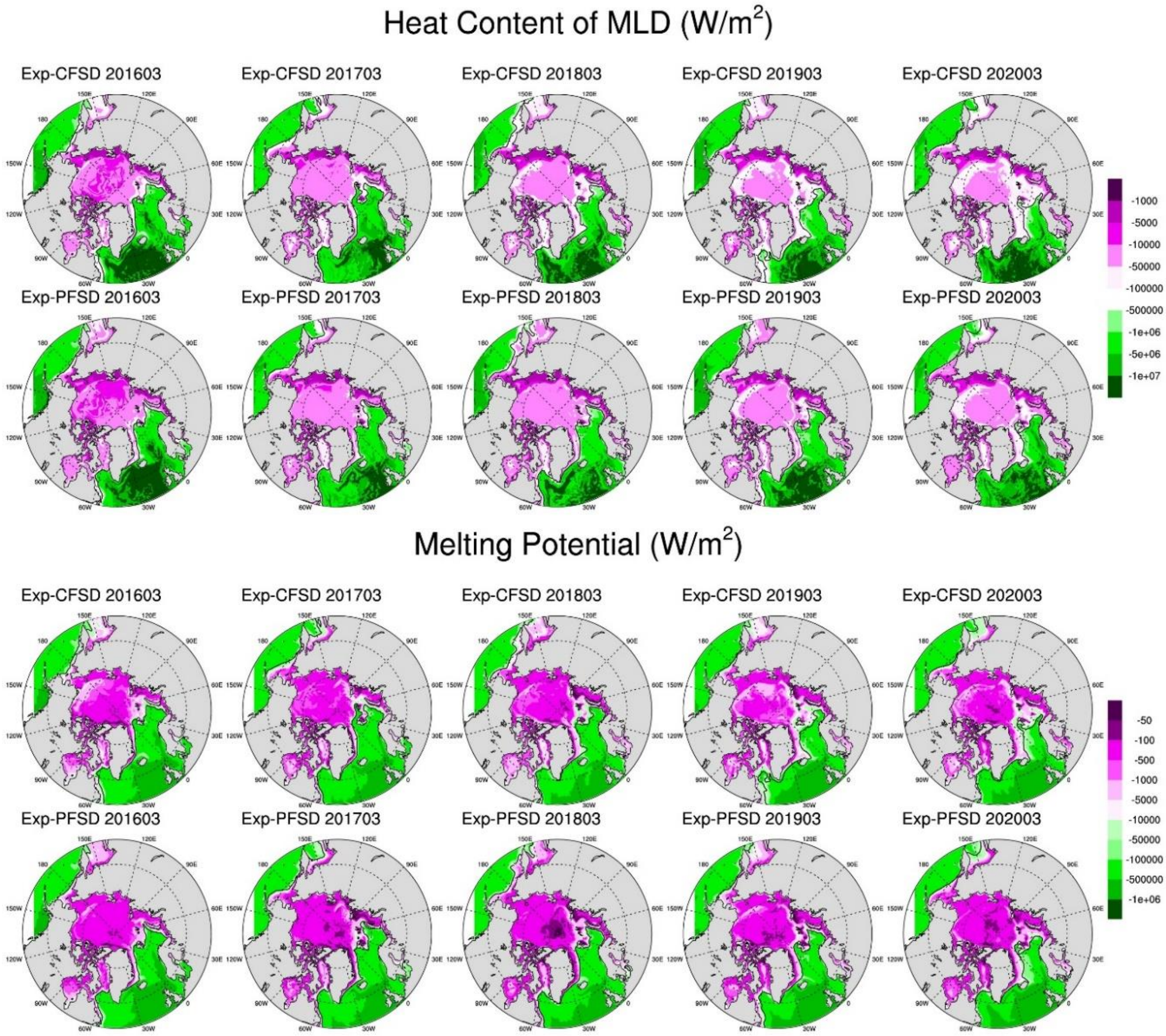

Figure 13 March-averaged heat content of MLD (top panel) and melting potential (bottom panel) of Exp-CFSD and Exp-PFSD for 2016-2020. Note: the black contour represents the average location of 15% ice concentration.

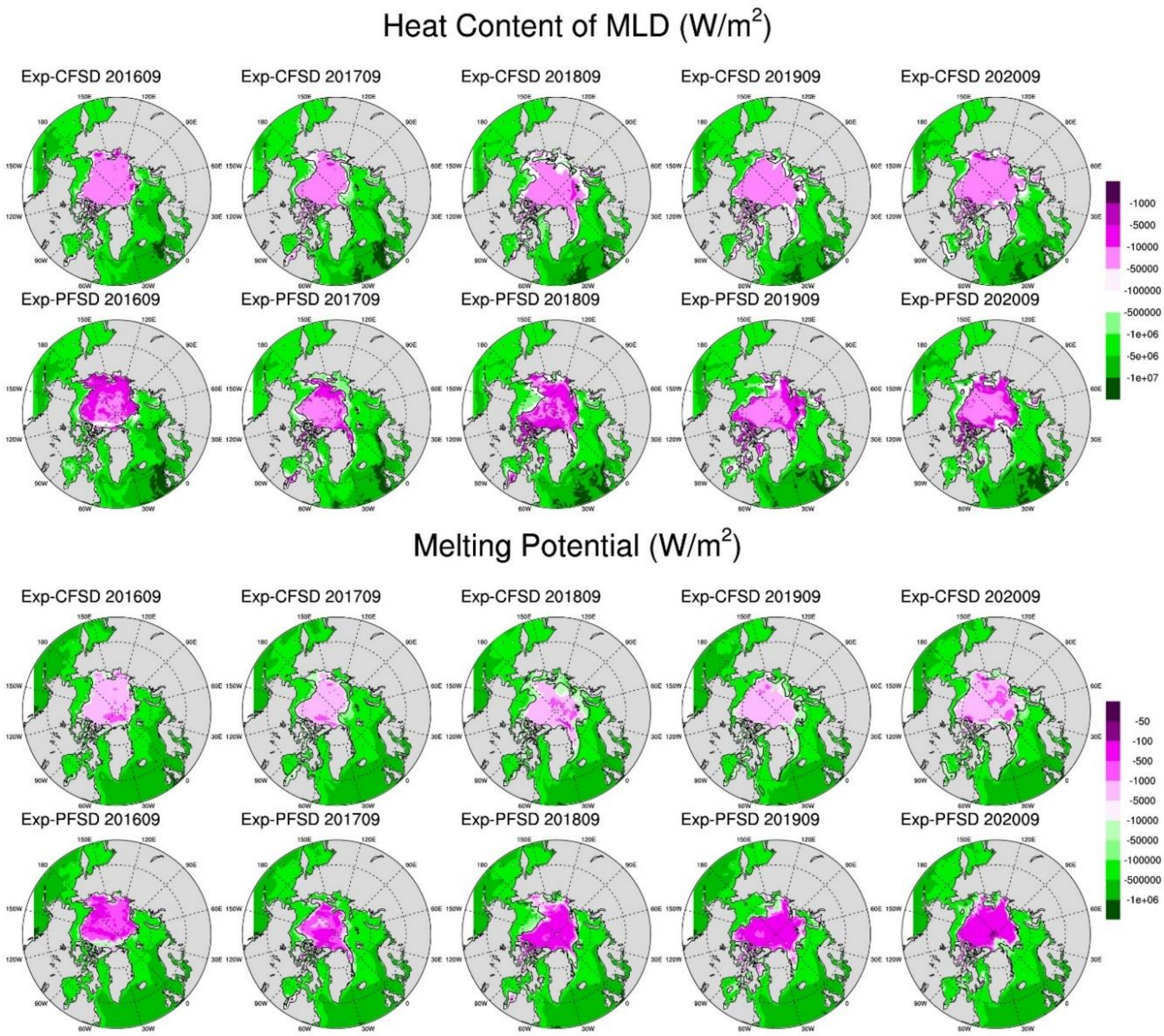

Figure 14 Same as Figure 13, but for September-averaged values.